



GEORG-AUGUST-UNIVERSITÄT
GÖTTINGEN

Fakultät für
Physik 

Bachelor's Thesis

Studien zur Identifikation von Top-Antitop-Paaren bei Variation der globalen Jet-Energie-Skala bei ATLAS am LHC

Studies for the Identification of Top-Antitop-Pairs with a variable global Jet Energy Scale at ATLAS/LHC

prepared at the 2. Physikalisches Institut
by Elina Fuchs from Göttingen

Thesis period: 6th April 2009 until 13th July 2009

Thesis number: II.Physik-UniGö-Bach-2009/07

Supervisors: Dr. Kevin Kröninger
Dipl. - Phys. Johannes Erdmann
Olaf Nackenhorst

First Referee: Prof. Dr. Arnulf Quadt

Second Referee: Prof. Dr. Ariane Frey

External Referee: Prof. Dr. Tony Liss (University of Illinois)

Abstract

In this bachelor's thesis the impact of the jet energy scale (JES) on the reconstruction of top pair ($t\bar{t}$) events at the ATLAS experiment is examined in the context of a kinematic fitting method. Based on a Maximum Likelihood approach, simulated $t\bar{t}$ events in the semileptonic decay channel with one electron and four jets are fitted with the JES as a free parameter. A requirement of equal top and antitop masses or a Breit-Wigner function centered at a fixed value for both top masses are used as kinematic constraints, respectively.

The estimated JES extracted from the first fit is used as a new *a priori* probability for a second fit. While the most significant improvement of the energy resolution is achieved by the first fit, the second fit particularly yields higher reconstruction efficiencies and a better top mass reconstruction. The two steps of this fitting procedure reduce the influence of the JES on the reconstructed variables.

Zusammenfassung

In dieser Bachelorarbeit wird der Einfluss der Jet-Energie-Skala (JES) auf die Rekonstruktion von Top-Paaren am ATLAS-Experiment mit einem kinematischen Fit untersucht. Dabei werden simulierte, semileptonisch in ein Elektron und vier Jets zerfallende $t\bar{t}$ Ereignisse nach dem Maximum-Likelihood-Prinzip kinematisch gefittet, wobei die JES als freier Parameter variiert wird. Als kinematische Zwangsbedingungen werden entweder gleiche Massen des Top- und Antitop-Quarks oder eine Breit-Wigner-Verteilung beider Topmassen verwendet.

Die Bestimmung der geschätzten JES aus dem Fit dient als neue *a priori* Wahrscheinlichkeit für einen zweiten Fit. Während sich im ersten Fit die Energieauflösung am deutlichsten verbessert, erzielt der zweite Fit vor allem höhere Rekonstruktionseffizienzen und eine bessere Topmassen-Rekonstruktion. Insgesamt verringern die beiden Schritte des Fittens den Einfluss der JES auf die rekonstruierten Größen.

Contents

1	Introduction	1
2	The Top Quark in the Context of the Standard Model	3
2.1	A Brief Summary of the Standard Model	3
2.1.1	Particles	3
2.1.2	Interactions	5
2.2	Overview over the Top Quark	7
2.2.1	Top Quark Properties	7
2.2.2	Top Quark Production at Hadron Colliders	9
2.2.3	Top Quark Decay	10
3	The ATLAS Detector at the LHC	13
3.1	The ATLAS Detector	15
3.2	Energy Resolution	16
3.3	Jet Energy Scale	17
4	Generation of the Events	19
4.1	Generation of The Monte Carlo Sample	19
4.2	Smearing of the Energies	19
5	Kinematic Fitting	21
5.1	Maximum Likelihood	21
5.2	Fit Parameters	22
5.3	Output Files	24
6	Results	25
6.1	Energy Resolution before the Fit	25
6.2	Results of the First Fit	27
6.3	Determination of the Global Jet Energy Scale	32

Contents

6.4	Second Fit	35
6.4.1	a priori Probabilities	35
6.4.2	Results of the Second Fit	36
6.5	Development of the JES Dependence	39
7	Conclusion	41
7.1	Summary	41
7.2	Outlook	42
A	First Appendix: Plots	43
	Nomenclature	49
	Bibliography	51
	List of Figures	55
	List of Tables	57

1 Introduction

The question about the world's constitution of smallest components has mattered to humans from the Greek antiquity until now. The principles of experiments in the field of *High Energy Physics* are collisions of strongly accelerated particles and the detection of their decay products from which conclusions about the particles and processes can be drawn. The smaller the scale of investigation is, the higher energies and larger colliders are required to study the properties and interactions of elementary particles in collision experiments. The Large Hadron Collider (LHC) provides the potential to test today's *Standard Model of Particle Physics (SM)* at high precision and search for the up to now undetected Higgs bosons, but also to look for new physics beyond the SM, for example, testing supersymmetric theories and searching for Dark Matter.

Especially the top quark with its extremely short lifetime of the order of 10^{-25} s and huge mass of the order of a gold atom is a field of strong interest. For example, it is important to measure its mass very precisely because the top mass constrains the prediction of the SM Higgs boson mass. But one of the dominating systematic uncertainties at hadron colliders is the determination of the jet energy scale (JES). In particular in first data, top events can be used for the calibration of the detector. In this thesis the jet energy scale is therefore included in a kinematic fit which can be used for the reconstruction of top-antitop pairs.

1 Introduction

The following chapter gives an introductory review of the *Standard Model of Particle Physics* with emphasis on the top quark. Chapter 3 will describe the experimental setup of the ATLAS detector at the LHC and the jet energy scale is introduced. Chapter 4 contains a description of the events generated by a Monte Carlo simulation and used as "measured data" after smearing. In chapter 5 the procedure of the kinematic fit based on a Likelihood approach is presented. Chapter 6 shows the results of the fit comparing the energy resolution, the reconstructed top mass and the reconstruction efficiency before the fit and after two steps of fitting, respectively. Finally, the procedure and the results are summarized and an outlook for future studies is given in chapter 7.

2 The Top Quark in the Context of the Standard Model

This chapter gives a short introduction to the field of physics this analysis of top-antitop-decays is based on. A summary of the Standard Model of Particle physics is followed by a discussion of the properties of the top quark and its production and decay processes.

2.1 A Brief Summary of the Standard Model

The *Standard Model of Particle Physics* [1] describes particles and their interactions. It is based on a quantum field theory and gauge symmetries which lead to the fundamental interactions as the electromagnetic, weak and strong forces. It comprises of twelve initially massless fermions (spin $s = 1/2$), namely six quarks and six leptons together with their antiparticles. The interactions are mediated by gauge bosons (spin $s = 1$). The particles acquire mass by the so-called Higgs mechanism. However, the manifestation of the Higgs field – the Higgs boson – has not yet been observed.

2.1.1 Particles

The fermions (spin $s = \frac{1}{2}$) are arranged in three families, each, forming left-handed weak isospin (I_3) doublets and right-handed singlets. While each lepton doublet contains one uncharged neutrino (ν_e, ν_μ, ν_τ) and one lepton with the elementary charge $Q = e$ (e, μ, τ), both quarks in a quark doublet are charged. Those with positive electric charge $Q = +\frac{2}{3}$ are called up-type (u, c, t), those with negative charge $Q = -\frac{1}{3}$ are called down-type (d, s, b). The masses of the particles range from the nearly massless neutrinos over $m_e \approx 0.511 \text{ MeV}/c^2$ to $m_t = 173.1 \pm 1.3 \text{ GeV}/c^2$ [2] as

2 The Top Quark in the Context of the Standard Model

can be seen in tab. (2.1). The antiparticles have the same mass¹ as the corresponding particles, but opposite charge and weak isospin. All particles are represented by fermionic or bosonic fields, respectively.

Table 2.1: Mass and lifetime of leptons and quarks [3], m_t from [2].

Lepton	Mass m [MeV]	Lifetime τ	Quark	Mass m [MeV]	Lifetime τ [s]
e	0.510998910(13)	$\geq 4.6 \cdot 10^{26}$ yr	u	1.5-3.3	
μ	105.658367(4)	$2.197019(21) \cdot 10^{-6}$ s	d	3.5-6.0	
τ	1776.84(17)	$290(1).6 \cdot 10^{-15}$ s	c	1270_{-110}^{+700}	
ν_e	$\leq 2 \cdot 10^{-6}$		s	104_{-34}^{+26}	$\sim 10^{-23}$
ν_μ	$\leq 2 \cdot 10^{-6}$		t	173100(1300)	$5 \cdot 10^{-25}$
ν_τ	$\leq 2 \cdot 10^{-6}$		b	4200_{-70}^{+170}	

The following table (2.2) gives an overview of the particle properties like the spin s , the third component of the isospin I_3 , the electromagnetic charge Q , the weak hypercharge $Y = 2(Q - I_3)$ and the colour charge C .

The weak q' and the mass eigenstates q are not equal, but they are linear combinations of each other. The coefficients are written in a matrix. In case of mixing of the first two quark generations only, this is the 2×2 CABIBBO matrix (1963) with the Cabibbo angle θ_C . In 1973 CABIBBO, KOBAYASHI and MASKAWA extended the quark² mixing to three generations with the so called *CKM matrix* [4]. While a unitary 2×2 matrix contains only two real parameters, a 3×3 matrix has three real and one imaginary parameter, which is responsible for CP-violation. The CKM matrix V parametrizes the mixture of mass eigenstates d, s, b to weak eigenstates³ d', s', b' :

$$\begin{pmatrix} d' \\ s' \\ b' \end{pmatrix} = \begin{pmatrix} V_{ud} & V_{us} & V_{ub} \\ V_{cd} & V_{cs} & V_{cb} \\ V_{td} & V_{ts} & V_{tb} \end{pmatrix} \begin{pmatrix} d \\ s \\ b \end{pmatrix}$$

Unitarity of V interdicts flavour changing neutral currents.

¹if CPT is conserved

²Neutrino mixing is described by the PONTECORVO-MAKI-NAKAGAWA-SAKATA (PMNS) matrix.

³The mixture refers to the down-type quarks, but could equivalently also be based on the up-type quarks.

Table 2.2: Fundamental particles in the Standard Model [3] and their properties spin s , weak isospin I_3 , electric charge Q , weak hypercharge Y and colour charge C . q' denotes the weak eigenstates.

Particles	s	I_3	$Q[e]$	Y	C		
Fermions							
$\begin{pmatrix} \nu_e \\ e^- \end{pmatrix}_L$	$\begin{pmatrix} \nu_\mu \\ \mu^- \end{pmatrix}_L$	$\begin{pmatrix} \nu_\tau \\ \tau^- \end{pmatrix}_L$	$\frac{1}{2}$	$\begin{pmatrix} +\frac{1}{2} \\ -\frac{1}{2} \end{pmatrix}$	$\begin{pmatrix} 0 \\ -1 \end{pmatrix}$	-1	0
$\begin{pmatrix} u \\ d' \end{pmatrix}_L$	$\begin{pmatrix} c \\ s' \end{pmatrix}_L$	$\begin{pmatrix} t \\ b' \end{pmatrix}_L$	$\frac{1}{2}$	$\begin{pmatrix} +\frac{1}{2} \\ -\frac{1}{2} \end{pmatrix}$	$\begin{pmatrix} +\frac{2}{3} \\ -\frac{1}{3} \end{pmatrix}$	$+\frac{1}{3}$	r, g, b
e_R	μ_R	τ_R	$\frac{1}{2}$	0	-1	-2	0
u_R	c_R	t_R	$\frac{1}{2}$	0	$+\frac{2}{3}$	$+\frac{4}{3}$	r, g, b
d'_R	s'_R	b'_R	$\frac{1}{2}$	0	$-\frac{1}{3}$	$-\frac{2}{3}$	r, g, b
Gauge Bosons							
γ			1	0	0	0	0
Z^0			1	0	0	0	0
W^\pm			1	± 1	± 1	0	0
$8 g$			1	0	0	0	r, g, b

2.1.2 Interactions

The theory of the electromagnetic, weak, and strong interactions is mathematically expressed by local gauge symmetries, i.e. the invariance of the Lagrangian under a transformation of a certain Lie-group. Relevant Lie-groups are here the (special) unitary groups. The dimension of any $SU(N)$ group is $N^2 - 1$ which equals the numbers of generators and gauge fields identified with the interaction.

In case of quantum electrodynamics the corresponding Abelian Lie-group $U(1)_{em}$ consists of phase transformations $\Psi(x) \rightarrow \Psi'(x) = e^{i\alpha}\Psi(x)$ and is connected to the field B_μ with a coupling constant g . On the contrary, $SU(2)_{weak}$ is generated by the three Pauli matrices σ^i with $i \in 1, 2, 3$ which do not commute. Hence, the $SU(2)$ is not Abelian. There are three gauge fields W_μ^i with the coupling strength g' . The weak and electromagnetic interaction are unified to the symmetry group $SU(2)_L \otimes U(1)_Y$ which contains the $U(1)_{em}$ as a subgroup. L denotes the exclusive coupling to left-handed particles and $Y = 2(Q - I_3)$ is the weak hypercharge. The exchange bosons A_μ and Z_μ are obtained from linear combinations of the gauge fields B_μ and W_μ^3 . The angle between the two is called WEINBERG angle with

2 The Top Quark in the Context of the Standard Model

$\sin^2(\theta_W) = \frac{g'^2}{g^2+g'^2} = 0.23$. It represents the electroweak mixing:

$$W_\mu^\pm = \frac{1}{\sqrt{2}} (W_\mu^1 \mp W_\mu^2) \quad \leftrightarrow W^\pm \quad (2.1)$$

$$A_\mu = +B_\mu \cos(\theta_W) + W_\mu^3 \cos(\theta_W) \quad \leftrightarrow \gamma \quad (2.2)$$

$$Z_\mu = -B_\mu \sin(\theta_W) + W_\mu^3 \cos(\theta_W) \quad \leftrightarrow Z^0 \quad (2.3)$$

Breaking the $SU(2)_L \otimes U(1)_Y$ symmetry by the ground states leads to the mass creating Higgs mechanism. An additional field – the HIGGS-field – needs to be introduced. The coupling strength of a particle to the Higgs-field is proportional to its mass.

The symmetry group $SU(3)_C$ of quantum chromodynamics is generated by the eight GELL-MAN matrices λ^a . Here, the index C indicates the colour charge red, green, blue. There are eight gluon fields $G_{\mu\nu}^a$, with $a \in 1, \dots, 8$ which carry a colour charge themselves. Combining the electroweak and strong interaction results in the symmetry group of the Standard Model:

$$SU(3)_C \otimes SU(2)_L \otimes U(1)_Y$$

All particles participate in the weak interaction, whereas only charged particles can interact electromagnetically. Gluons only couple to colour-charged particles, i.e., to quarks and to themselves. While the weak gauge bosons can couple to themselves, too, the photon, however, is uncharged so that a self-interaction is not possible. Mathematically, this is due to the Abelian nature of the group $U(1)$.

The masses and total decay widths of the exchange bosons as well as the relative interaction strength are listed in table (2.3). Due to renormalization of the charge, the coupling strengths are not constant, but they run with the energy. It increases for higher energies in the electromagnetic case. The strong coupling, by contrast, diverges at low and decreases at high energies which is known as *confinement* and *asymptotic freedom*. For this reason no free quarks can be observed.

Despite the excellent accordance of the SM predictions with current precision experiments the Standard Model is not regarded as a complete theory. Neither the unification of the electromagnetic, weak and strong interaction nor the implementation of gravity can be accomplished within the framework of the SM. Furthermore, the matter-antimatter-imbalance and Dark Matter require more sophisticated theories which are to be tested at the LHC.

Table 2.3: Coupling strength, mass and lifetime of the gauge bosons [3].

Particle	γ (photon)	Z^0	W^\pm	g (8 gluons)
Interaction	electromagnetic	weak	weak	strong
Relative strength	10^{-2}	10^{-6}	10^{-6}	1
Mass m [GeV]	0	91.1876(21)	80.398(25)	0
Total width Γ [GeV]	0	2.4952(23)	2.141(41)	0

2.2 Overview over the Top Quark

Although the top quark had already been predicted when the 3×3 CKM matrix was postulated in 1973, it was only discovered in $t\bar{t}$ pair production in 1995. The CDF [5] and D0 collaborations [6] found the heaviest and last of the six quarks at the Tevatron proton antiproton collider in Run I with $\sqrt{s} = 1.8$ TeV. Recently in 2009, both collaborations stated the dicoverly of electroweak single top quark production at the Tevatron in Run II with $\sqrt{s} = 1.96$ TeV [7] [8]. The large mass of $m_t = 173.1$ GeV/ c^2 and the extremely short lifetime of $\tau_t \approx 5 \cdot 10^{-25}$ s of this quark impeded its discovery. In the following, the properties, production mechanisms and decay schemes of the top quark will be described.

2.2.1 Top Quark Properties

The top quark is the weak isospin partner of the bottom quark. Although not measured experimentally, it is assumed to have a charge of $Q = +\frac{2}{3}$ and a spin of $s = \frac{1}{2}$.

Mass There are different definitions for the top mass. One has to distinguish between the on-shell or pole mass and the concept of mass in various renormalization schemes. On the one hand, the pole mass is understood as the real part of the complex pole $\sqrt{p^2} = m_t - \frac{i}{2}\Gamma_t$ of the quark propagator in a finite-order perturbation theory [9]. On the other hand, the *Modified Minimal Subtraction* scheme ($\overline{\text{MS}}$) removes infinities and finite terms from the divergent mass as a renormalization. The pole and $\overline{\text{MS}}$ mass can differ by about 10 GeV [9].

Experimentally, the top mass is typically reconstructed from its 4-momentum $m = \sqrt{p_\mu p^\mu}/c^2$ by measuring the 4-momenta of the particles the top quark decays into (see section 3.3). Results from both Tevatron experiments CDF and D0 were combined

2 The Top Quark in the Context of the Standard Model

in order to yield the current world average of [2]

$$m_t^{world} = (173.1 \pm 0.6 \pm 1.1) \text{ GeV}/c^2.$$

The uncertainties refer to the statistical and systematic uncertainties, respectively. The main contribution to the systematic uncertainties originates from the jet energy scale (s. section 3.3). Comparing the total uncertainty

$$\sigma_{tot} = \sqrt{\sigma_{stat}^2 + \sigma_{syst}^2} = 1.25 \text{ GeV}/c^2$$

to the top mass yields a very high relative precision which exceeds the precision of other quark masses by far:

$$\sigma_{rel} = \frac{\sigma_{tot}}{m_t} = 0.72\%$$

Lifetime Due to its large mass, the top quark can decay into an on-shell W-boson and a b-quark with $V_{tb} \approx 1$ which results in an extremely short proper lifetime of

$$\tau_t = \frac{1}{\Gamma_t} \simeq 5 \cdot 10^{-25} \text{ s} < 3 \cdot 10^{-24} \text{ s} \simeq \tau_{had} = \frac{1}{\Lambda_{QCD}}.$$

Thus, the top quark decays before it can form hadrons. Therefore, toponium bound states (mesons of t and \bar{t}) do not exist. The total width $\Gamma = \frac{\hbar}{\tau}$ is proportional to $|V_{tb}|^2$ and depends on the ratio $\frac{m_W}{m_t}$. Neglecting the bottom mass and taking into account the leading order (LO) only, the width reads as follows [10]:

$$\Gamma(t \rightarrow Wb) = \frac{G_F}{8\pi\sqrt{2}} m_t^3 |V_{tb}|^2 \left(1 - 3 \left(\frac{m_W}{m_t} \right)^4 + 2 \left(\frac{m_W}{m_t} \right)^6 \right)$$

The result according to [9] is $\Gamma_t^{Born} = 1.44 \text{ GeV}$. The QCD corrections can be written in an expansion of the Born approximation in terms of α_s :

$$\Gamma_t = \Gamma_t^{Born} (1 - 0.81\alpha_s - 1.81\alpha_s^2)$$

Owing to the running coupling $\alpha_s = \alpha_s(m_t)$, the width increases significantly with the top mass, e.g., [3] [11]

$$\Gamma_t(m_t = 160 \text{ GeV}/c^2) = 1.02 \text{ GeV}/c^2, \quad \Gamma_t(m_t = 180 \text{ GeV}/c^2) = 1.56 \text{ GeV}/c^2.$$

2.2.2 Top Quark Production at Hadron Colliders

Top quarks can be produced in $t\bar{t}$ pairs or as a single top quark.

$t\bar{t}$ Pair production Top pairs are produced via the strong interaction, either by quark-antiquark annihilation or by gluon fusion. At high energies, this can be described by perturbative QCD interactions of quarks and gluons as the constituents of the colliding hadrons [12]. In leading order there are three Feynman diagrams with $gg \rightarrow t\bar{t}$ and one for $q\bar{q} \rightarrow t\bar{t}$, which are shown in fig. (2.1).

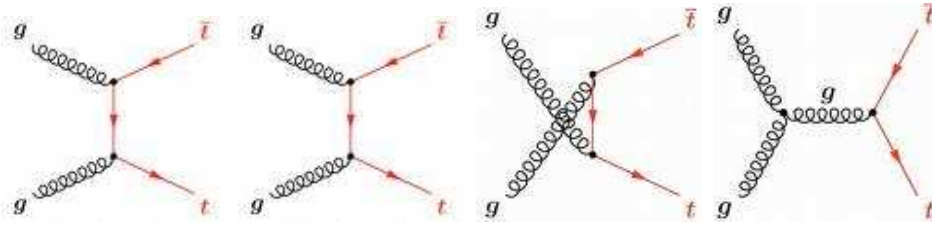


Figure 2.1: Leading order diagrams for strong $t\bar{t}$ production with $q\bar{q}$ (left) annihilation and gg fusion [13].

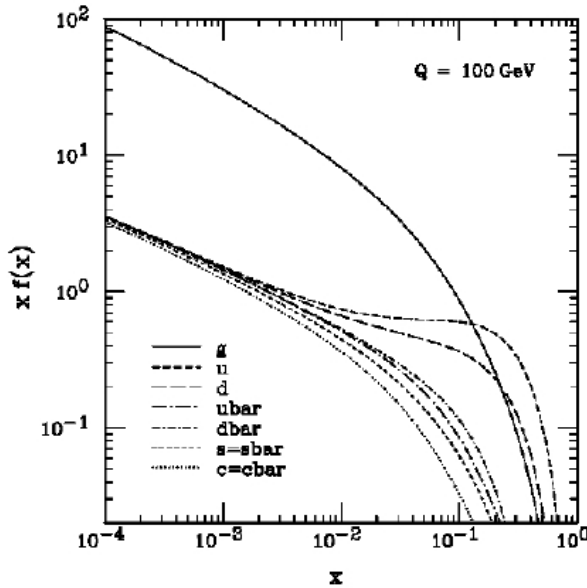


Figure 2.2: Parton density functions of $Q = 100$ GeV [14].

The relative contributions to the total cross section depend on the center-of-mass energy because of the parton density function. The BJORKEN- x represents the ratio of a parton momentum to the total momentum. At small x the parton distribution of the gluons dominates over the quarks. That means the $t\bar{t}$ production is dominated by $q\bar{q}$ annihilation at the Tevatron. Conversely, at the LHC a predominant production via gg -fusion is expected on account of the higher center-of-mass energy. The relative contribution of both production mechanisms are summarized in table (2.4) [9] and the parton distributions can be found in fig. (2.2).

Table 2.4: Contribution of $q\bar{q}$ annihilation and gg fusion to the total $t\bar{t}$ production cross section.

experiment	s [TeV]	$q\bar{q}$ [%]	gg [%]
Tevatron Run I	1.8	85	15
Tevatron Run II	1.96	90	10
LHC (2009/10)	10		
LHC (2010?-..)	14	10	90

Single top Single top quarks can be produced via the weak interaction. The processes can be mediated by a W-boson in the t- or s- channel. An associated production of a top quark and W-boson is also possible [10]. All these processes are proportional to $|V_{tb}|^2$ which allows for its direct measurement. In addition, the top quarks produced in this way are highly polarized so that charged weak currents can be investigated. But these signatures suffer from a larger background and a smaller cross section compared to the $t\bar{t}$ production.

2.2.3 Top Quark Decay

From unitarity of the CKM matrix

$$(V^*V)_{ik} = \sum_j V_{ij}^* V_{jk} = \delta_{ik} \quad (2.4)$$

for $i = k = t$ and $j = d, s, b$ it can be concluded that

$$V_{td}^* V_{dt} + V_{ts}^* V_{st} + V_{tb}^* V_{bt} = |V_{td}|^2 + |V_{ts}|^2 + |V_{tb}|^2 = 1. \quad (2.5)$$

V is approximately diagonal which becomes apparent in the Wolfenstein parametrization [15]. Measurements [16] revealed $V_{tb} \in [0.9990, 0.9993]$. Consequently, top quarks decay almost exclusively into an (anti-)bottom quark and a W^\pm boson. Subsequently, both b-quarks of the $t\bar{t}$ decay hadronize to jets which contain B mesons and can thus be distinguished from jets originating from light quarks. Further, each W-boson can either decay into two light quarks q_1, \bar{q}_2 which then form jets (*hadronic decay*), or into a charged lepton and its corresponding antineutrino (*leptonic decay*). Since both W-bosons decay independently and the order of the first and second W-boson does not influence the final state, the two decay channels can be combined in three ways: *dileptonic*, *semileptonic* (*lepton+jets*) and *all-jets*. The branching ra-

tios (BR) for the combined $t\bar{t}$ decays are obtained from multiplying the probabilities of the independent channels, taking into account the colour factors $N_C^{lep} = 1$ and $N_C^{had} = 3$ (see table 2.5).

Table 2.5: Branching ratios of the final states from a decay of a W^+ , analogously for W^- .

Final states	$e^+\nu_e$	$\mu^+\nu_\mu$	$\tau^+\nu_\tau$	$u\bar{d}$	$c\bar{s}$
N_C	1	1	1	3	3
BR	1/9	1/9	1/9	1/3	1/3

The $\tau + \nu_\tau$ final states are difficult to identify and they are therefore neglected. Consequently, the probabilities of leptonic and hadronic decays are:

$$P(lep) = \frac{2}{9} \qquad P(had) = \frac{2}{3}$$

In the following, the three different channels are characterized [9]:

- **dileptonic:** Both W-bosons decay leptonically (e or μ) so that the branching ratio $BR = \left(\frac{2}{9}\right)^2 = \frac{4}{81}$ is rather small. The signature consists of two oppositely charged, isolated leptons with a high transversal momentum p_T , at least two jets from b-quarks and a large amount of missing transversal energy E_T from the undetected neutrino. Although the clear signature has little background, the missing E_T of the two unobserved neutrinos prevents a complete reconstruction.
- **semileptonic:** If one W-boson decays leptonically and the second hadronically, the branching ratio $BR = 2 \cdot \frac{2}{9} \cdot \frac{2}{3} = \frac{8}{27}$ is larger, but there is also more background. The neutrino momentum can be reconstructed from momentum and energy conservation. The signature is compound of one charged isolated, high p_t lepton, at least four jets (two originating from b-quarks) and large missing energy.
- **all-jets:** The branching ratio for the hadronic decay of both W-bosons $BR = \left(\frac{2}{3}\right)^2 = \frac{4}{9}$ is the highest, but a large QCD multijet background superposes the at least six jets signature. All particles in the final state can be detected so that no missing energy needs to be taken into consideration.

The analysis presented in the following has been performed assuming the semileptonic channel with one electron and four jets.

3 The ATLAS Detector at the LHC

The Large Hadron Collider (LHC) [17] is a proton-proton (pp) collider at CERN (Geneva). It is built to search for the up to now undetected Higgs boson, to look for physics beyond the Standard Model (SM) like supersymmetry, Dark Matter and extra dimensions and to test the SM at high precision. The LHC accelerator was already conceived in the 1980s and approved for construction by the CERN Council in 1994. The first particle beam was accelerated in September 2008 and the LHC is expected to provide pp collisions in the fall 2009.

The LHC was designed to collide two proton beams at a center-of-mass energy of $\sqrt{s} = 14 \text{ TeV}$ at an instantaneous peak luminosity of $10^{34} \text{ cm}^{-2}\text{s}^{-1}$. Due to limited currents in the magnets, the LHC is forced to operate at lower energy (10 TeV) and less luminosity in the beginning. The luminosity is supposed to be achieved by 2808 proton bunches with approximately 10^{11} protons in each bunch. Assuming the design technical characteristics [17], a bunch crossing is expected every 25 ns with approximately 23 interactions [18] per bunch crossing. Thus, nearly one billion pp interactions per second are expected.

Before entering the 27 km circumference LHC accelerator, the protons are pre-accelerated in a chain of several smaller linear and ring accelerators as shown in figure (3.1). The particles are accelerated by radio frequency cavities located along the beam pipe with an ultrahigh vacuum of 10^{-10} mbar. While dipole magnets bend the beam around the ring, quadrupole magnets are responsible for the focusing. The necessary strong magnetic fields are realized by superconducting coils which require as low temperatures as 1.9 K. This cooling is obtained with superfluid helium.

Four experiments are located at the four interaction points along the beam pipe of the LHC.

- **ALICE (A Large Ion Collider Experiment)** [20] collides lead ions and produces a quark-gluon-plasma in order to study the conditions shortly after the Big Bang before the confinement of gluons and quarks.
- **LHCb (Large Hadron Collider Beauty experiment)** [21] focuses on the

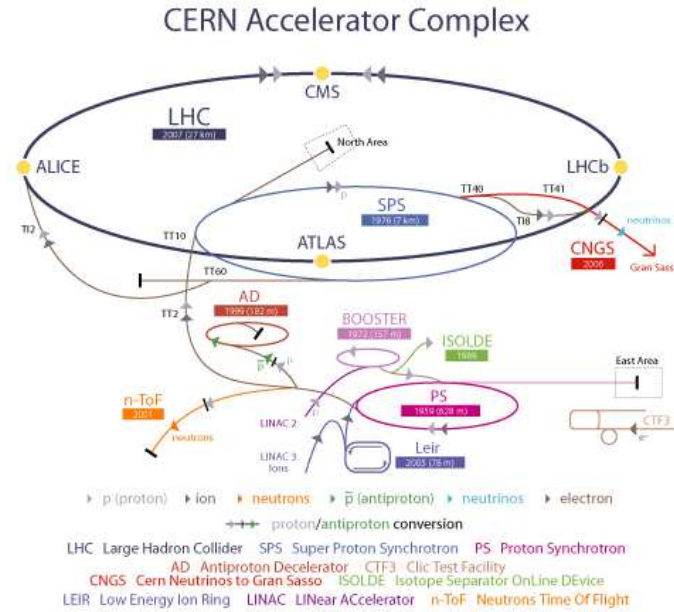


Figure 3.1: CERN accelerators [19]. The particles are pre-accelerated before entering the LHC.

interaction of b-quarks to investigate the CP violation and matter-antimatter-asymmetry in the B-sector. Several sub-detectors detect mainly forward particles.

- **CMS (Compact Muon Solenoid) with TOTEM (TOTal Elastic and diffractive cross section Measurement)** [22] is one of the two general-purpose detectors. The trajectories of charged particles are bent by a 4 T magnetic field produced by a superconducting solenoid coil. They are tracked by strip and pixel silicon sensors. Furthermore, there are electromagnetic and hadronic calorimeters and muon detectors (drift tubes, cathod strip chambers and resistive plate chambers). With a length of 21 m, 15 m in diameter and a weight of 14000 t, CMS is smaller and heavier than the ATLAS detector.¹
- **ATLAS (A Toroidal LHC Apparatus) with LHCf (forward)** [23] is also a general-purpose detector. 44 m long and 25 m in diameter, ATLAS is the largest detector for particle physics ever built. It weights 7000 t. Its properties will be discussed in the following chapter in more detail. LHCf consists of two detectors which measure cascades of particles similar to cosmic rays in the

¹Therefore, it earns the name "compact".

very forward region.

ATLAS and CMS are two multi-purpose detectors with the same aims of studies, but with different techniques in order to cross-check each other's results.

3.1 The ATLAS Detector

ATLAS [18] consists of several subdetectors (see fig. 3.1): the inner detector, the calorimeters, the muon spectrometer, and the solenoidal and toroidal magnets.

The innermost part contains the *pixel detector* with over 80 million rectangular pixels. These provide a spatial resolution of the order of μm . The *Semi-Conductor Tracker (SCT)* uses layers of silicon microstrip sensors and has 6.3 million read-out channels. The *Transition Radiation Tracker (TRT)* consists of 4 mm diameter straw tubes. Pions and electrons traversing the detector can be distinguished by their transition radiation. The timing of the pulse allows the determination of the distance between the particle track and the wire with a precision of 0.17 mm. In general, tracking and vertexing belong to the identification of particles.

There are different types of calorimeters. The *Liquid Argon Calorimeter* can be specified in the *electromagnetic* and *hadronic* one and the *Liquid Argon Forward Calorimeter*. Furthermore, there is a *Hadronic Tile Calorimeter*. In *sampling calorimeters*, passive absorber material and active material alternate. The active medium is equipped with a read-out system and it can be realized by scintillators, semiconductors or gas chambers. Altogether they form the calorimeter system. It surrounds the inner detector and measures the energy deposited by electrons, muons, photons and hadrons, respectively, based on their interaction with matter. The muon spectrometer as the outermost layer measures the momenta of muons with a precision of $\frac{\sigma_{p_T}}{p_T} \leq 10\%$ [24]. Divided into high precision and trigger chambers, it consists of gas-filled *Monitored Drift Tubes (MDT)* for the determination of muon positions by the drift time of electrons, the *Thin Gap Chambers (TGC)* for the identification of energetic muons, *Cathode Strip Chambers (CSC)* for the muon trajectories and *Resistive Plate Chambers (RPC)* with a good timing resolution.

The central solenoid with a peak magnetic field of 2 T is located outside of the inner detector. A large system of air-core toroids is arranged outside the calorimeter volume. The inhomogenous magnetic field with a peak in the end-cap regions of ~ 1 T bends the trajectory of the muons.

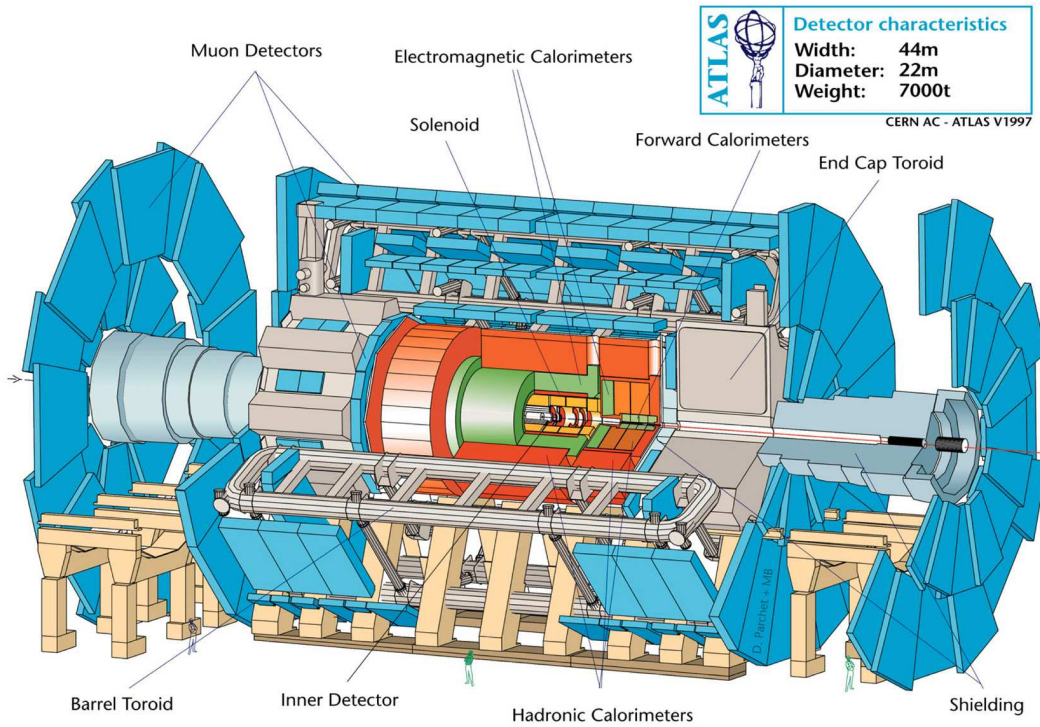


Figure 3.2: The ATLAS detector with the inner detector, the electromagnetic and hadronic calorimeters, the muon system and the toroidal and solenoidal magnets.

3.2 Energy Resolution

There are different contributions to the uncertainty of the energy measured in the calorimeter. As the deposited energy E is proportional to the number of ionized particles N and counting experiments follow Poisson statistics ($\sigma_N = \sqrt{N}$), the relative statistical error of the energy reads:

$$\frac{\sigma_E^{stat}}{E} = \frac{a}{\sqrt{E}}$$

where a stands for statistical fluctuations like intrinsic shower fluctuations and photoelectron statistics [3]. In addition, a constant term b takes systematic uncertainties such as detector non-uniformity and calibration inaccuracy into account. Moreover, a noise term c is due to instrumental effects like pedestal shifts so that the relative

energy uncertainty of the calorimeter is hence given as:

$$\frac{\sigma_E}{E} = \frac{a}{\sqrt{E}} \oplus b \oplus \frac{c}{E} \equiv \sqrt{\frac{a^2}{E} + b^2 + \frac{c^2}{E^2}} \quad (3.1)$$

The term $\frac{c}{E}$ can be neglected at high energies so that the systematic term dominates. The noise term, on the contrary, has the largest influence at lower energies. The most important contribution to the systematic uncertainty - the jet energy scale - will be defined in the next section.

3.3 Jet Energy Scale

The energy recorded by a calorimeter is not necessarily the correct energy of a jet, but it can be stretched or clinched by a factor, the so-called *Jet Energy Scale (JES)* which is specific for each detector and for the calibration, the jet algorithm and clustering. So the measured energy E_m must be scaled with the JES α :

$$E_m \rightarrow \frac{E_m}{\alpha}.$$

For calibrating the JES in an experiment, the knowledge of the W mass can be used to scale the energy of two light quarks as $p_W = p_{q1} + p_{q2}$ and $m_W = \sqrt{(p_{q1} + p_{q2})^2} = 80.4 \text{ GeV}/c^2$. This usage of the W mass constraint is one kind of *in-situ* calibration. The JES uncertainty can be sub-divided into more specified components as in analyses of the Tevatron [2]. But several of the JES contributions must also be taken into consideration at other hadron colliders. The following listing gives some examples for experiment-independent JES uncertainties:

- uncertainties from the in-situ calibration;
- uncertainties arising from different detector responses for b-jets and light-quark jets including jet identification and b-jet tagging;
- the modeling of b-jets, light-quark fragmentation and out-of-jet/ out-of-cone corrections influences the interpretation of the JES;
- the calibration data sample limits the JES accuracy.

4 Generation of the Events

4.1 Generation of The Monte Carlo Sample

The following analysis uses Monte Carlo Samples (MC) of $t\bar{t}$ decays in the semileptonic channel (with an electron and four jets) on tree level. They are generated by MadEvent [25] which is based on MadGraph [26]. All Feynman rules for processes in first order of perturbation theory are implemented in MadGraph. After the choice of a model (here SM) and an initial and final state, MadGraph calculates the matrix elements on tree level for each process between those two given states which are allowed according to the chosen model. Subsequently, the square of the absolute value of the matrix elements is integrated over the phase space using Monte Carlo techniques. The amplitudes are complicated functions of the momenta with sharp peaks in different regions of the phase space. Hence, an efficient numerical integration requires an identification of the position of those peaks and a mapping onto different sets of variables, called "channels". The process-specific information about the mapping is delivered to the multi-purpose generator MadEvent. These samples are understood as the "true" data set.

4.2 Smearing of the Energies

Neglecting the terms b and c in eq. (3.1) and assuming that the true energy E_{true} is known¹ we get an energy resolution of

$$\frac{\sigma_E}{\sqrt{E_{true}}} = \frac{E - E_{true}}{\sqrt{E_{true}}} \quad (4.1)$$

¹as it is the case with Monte-Carlo samples

4 Generation of the Events

The "measured"² values are produced by smearing the generated jet energies (from light and b-quarks) according to a Gaussian distribution with $a_{\text{jets}} = 50\%$, electron energies with $a_{\text{el}} = 10\%$. According to the simplified energy resolution (4.1), the width is $\sigma = a \cdot \sqrt{E_{\text{true}}}$. Random numbers are generated to produce a Gauss function centered at the true energy E_{true} with a width of σ . Then these values are scaled with the jet energy scale (JES) α so that the probability P for the "measured" energy E_m reads:

$$\begin{aligned}
 P(E_m) &= \alpha \cdot E_{\text{smearred}} & (4.2) \\
 &= \alpha \cdot \frac{1}{\sigma \sqrt{2\pi}} \cdot e^{-\frac{(E_m - E_{\text{true}})^2}{2\sigma^2}} \\
 &= \alpha \cdot \frac{1}{a \sqrt{2\pi} E_{\text{true}}} \cdot e^{-\frac{(E_m - E_{\text{true}})^2}{2a^2 E_{\text{true}}}} & (4.3)
 \end{aligned}$$

Afterwards, the momenta are scaled with the ratio of the absolute values of the measured and true 3-momenta:

$$\begin{aligned}
 \beta &:= \frac{|\vec{p}_m|}{|\vec{p}_{\text{true}}|} = \frac{\sqrt{E_m^2 - m^2}}{\sqrt{E_{\text{true}}^2 - m^2}} & (4.4) \\
 \rightarrow p_{\text{measured}} &= (E_m, \beta \cdot p_{x,\text{true}}, \beta \cdot p_{y,\text{true}}, \beta \cdot p_{z,\text{true}})
 \end{aligned}$$

This ensures that the measured angles

$$\begin{aligned}
 \eta &:= \ln \left(\tan \left(\frac{\theta}{2} \right) \right) \quad \text{and} \\
 \phi &:= \arctan \left(\frac{p_y}{p_x} \right)
 \end{aligned}$$

are equal to the true ones. The z-axis is defined as the beam axis. η is called the *pseudorapidity* which depends on the polar angle θ measured from the z-axis. ϕ is the azimuthal angle in the plane perpendicular to the beam direction.

This smearing and scaling imitates a dummy detector with a well-known behaviour concerning the energy resolution. From the MadEvent sample 10000 smeared events are produced for each JES from 0.6 to 1.4 in steps of $\Delta JES = 0.1$.

²In the following, *measured* does not refer to real measured data, but to these smeared MC energies.

5 Kinematic Fitting

Physical parameters are estimated in a kinematic fit which is supposed to increase the precision. More information is gained by exploiting energy and momentum conservation at each vertex in the form of constraints. This is possible if the knowledge about the top decay is applied to kinematic calculations.

This is performed by the *Kinematic Likelihood (KL) Fitter* [27] which is based on ROOT [28] in C++, the *Bayesian Analysis Toolkit (BAT)* [29] and MINUIT for the optimization.

5.1 Maximum Likelihood

The kinematic fit aims at determining the most probable values for certain variables by maximizing a Likelihood function. Such a fit parameter has to be estimated depending on the underlying data set of N elements (x_1, x_2, \dots, x_N) by a so called *estimator* \hat{a} for the true value a . It can have the three independent properties [30]:

- \hat{a} is *consistent* $:\Leftrightarrow \lim_{N \rightarrow \infty} \hat{a} = a$ so that the accuracy improves for larger data sets.
- \hat{a} is *unbiased* $:\Leftrightarrow \langle \hat{a} \rangle = a$, which means there is no systematic shift to larger or smaller values. Every consistent estimator is unbiased for $N \rightarrow \infty$ (asymptotic limit).
- \hat{a} is *efficient* $:\Leftrightarrow$ the variance $V(\hat{a})$ is small, i.e. there are no large deviations.

The *Likelihood* $L(x_1, x_2, \dots, x_N; a) = \prod P(x_i; a)$ is a product of individual probabilities $P(x_i; a)$, i.e., the probability for the data set (x, \dots, x_N) given a [31]. a is estimated by $\hat{a}(x_1, \dots, x_N)$ and obtained by maximizing $L(x_1, \dots, x_N; a)$ (*Maximum Likelihood, ML*). ML estimators are usually biased for small N , but they are invariant under scale transformations: $f(\hat{a}) = f(a)$. The maximum of $L(\vec{x}; a)$ with respect to a is the same as the maximum of $L(\vec{x}; f(a))$ with respect to $f(a)$ [30].

5 Kinematic Fitting

On account of the monotony of the natural logarithm, $L(\vec{x}; a)$ is maximal if and only if $\ln(L(\vec{x}; a))$ is maximal, too. With sums instead of products, it is easier to compute the maximum of $\ln L$ generalized to m parameters $\{a_j\}_{j=1, \dots, m}$:

$$\frac{\partial \ln L(x_1, x_2, \dots, x_N; a_1, \dots, a_m)}{\partial a_j} = 0 \quad \forall j \quad (5.1)$$

In case of Gaussian distributions the method of the least squares

$$\chi^2 := \sum_{i=1}^N \left[\frac{y_i - f(x_i, a)}{\sigma_i} \right]^2$$

follows directly from the ML principle where a parameter dependent function $f(x, a) = y$ describes the relation between the two data sets $\{x_i\}_{i=1 \dots N}$ and $\{y_i\}_{i=1 \dots N}$ with given y-errors σ_i . The best choice of all parameters must fulfill $\frac{\partial \chi^2}{\partial a_j} = 0 \quad \forall j = 1 \dots m$.

5.2 Fit Parameters

Candidates for top-pair-events are reconstructed with a kinematic fit using a Likelihood approach. The KL Fitter estimates the energies of the four jets and the charged lepton as well as p_z of the neutrino. Furthermore, the jet energy scale is added as a new fit parameter. The Likelihood function equals the product of the four quark energy resolution functions, one energy resolution function of the lepton and the Breit-Wigner functions of the W-boson masses. The implementation of the jet energy scale takes place in the Likelihood. Here, the probability of the energy resolution which depends on the estimated E_{est} and measured energy E_m is divided by the JES α for reasons of parametrization and E_m is scaled as described in chapter (3.3):

$$p(E_{est}, E_m) \mapsto \frac{1}{\alpha} p\left(E_{est}, \frac{E_m}{\alpha}\right) \quad \Rightarrow \quad \frac{1}{\alpha} \int p\left(E_{est}, \frac{E_m}{\alpha}\right) dE_m = 1$$

The range in which JES_{est} is allowed to vary is limited to $[0.5 \cdot JES_{true}, 1.5 \cdot JES_{true}]$.

Mass Constraints Some physical constants in $[\text{GeV}/c^2]$ are (partially) delivered to the fit:

$$m_b = 4.7 \quad m_t = 170 \quad \Gamma_t = 1.5 \quad m_W = 80.4 \quad \Gamma_W = 2.1 \quad m_{\text{light quarks}} = 0$$

The information about m_W and Γ_W is used to constrain the momenta of the two light quarks and the two leptons, as their combined momenta must be in the range of the W mass and width. This option involves two constraints because the Breit-Wigner (BW) distribution of $m_{W^+} = m_{W^-}$ with the width Γ_W is used for both the hadronically and leptonically decaying W-boson.

In addition to the W mass, constraints on the top mass are also possible. Without any further input to the fit, the masses of the top m_t and the antitop $m_{\bar{t}}$ are treated independently. Yet, implying the invariance under CPT (charge conjugation, parity and time reflection) yields $m_t = m_{\bar{t}}$. However, the absolute value of m_t is not known in this so-called *Equal Mass Constraint (EM)*. The numerical realization of "equal" is in this case a normalized Gauss function of $m_t - m_{\bar{t}}$ around zero with a width approximating Γ_t . This requirement on m_t corresponds to one constraint.

Fixing the top and antitop mass to a Breit-Wigner (BW) function with a peak at $170 \text{ GeV}/c^2$ and a width of 2.1 GeV introduces one more piece of information to the fit. The Breit-Wigner constraint is strong and helpful for combinatorics on the one hand, but on the other hand, it renders a mass measurement impossible because the mass is fixed already.

Let N be the number of variables, M the number of fitted parameters and P the number of constraints. Then the number k of degrees of freedom in the fit increases with more constraints [32]:

$$k = N - M + P$$

In this case there are $N = 5$ measured energies $E_{bhad}, E_{blep}, E_{q1}, E_{q2}, E_{lepton}$. The z-component of the ν momentum $p_z(\nu)$ and the JES cannot be measured, but they are fitted so that $M = N + 2 = 7$. The number of constraints P depends on the applied constraints which can be switched on or off by flags in the KLFFitter.

Table 5.1: Degrees of freedom k in dependence of the number of constraints P .

Constraint	P	k	Fit
BW for m_W	2	0	not possible
BW for m_W plus equal top mass	3	1	possible, no more parameters
BW for m_W plus for m_t	4	2	possible with even one more parameter

In case of $k = 0$ there is either one solution of the system of equations or there is none. Accordingly, a fit is not necessary or not possible. That means that the KLFFitter cannot be used with the implemented JES without any constraint. But

without the JES the KLfitter can estimate the W mass. The equal mass constraint for the top has exactly as many constraints as needed for a fit. However, no more parameter can be added in this mode - unlike in case of the BW constraint for m_t . For example two different jet energy scales for light and b-quarks could be defined.

Combinatorics The four detected jets have to be assigned to the four quarks for which there are $|S_4| = 4! = 24$ permutations. But interchanging the two indistinguishable light quarks leaves the Likelihood invariant since the hadronic W mass

$$m_{W_{\text{had}}} = m_{q_1} + m_{q_2} = m_{q_2} + m_{q_1}$$

does not depend on the order of the indices of the two light quarks q_1, q_2 . For this reason the switched permutation indices are removed and the number of physically relevant combinations reduces to 12. For each combination the parameters are fitted separately and the Likelihood is calculated. That combination with the highest value for the Likelihood is labelled as the best permutation, which is not necessarily the true combination.

5.3 Output Files

All values are saved in ROOT trees. The tree "Truth" contains the MC-generated events, the values in the tree "Measured" are smeared as mentioned in section (3.4) and "Model" is the tree for the fitted results. While in the truth-tree the jets are only called "jet 1,...,jet 4", they are assigned as $b_{\text{had}}, b_{\text{lep}}, q_{\text{up}}, q_{\text{down}}$ in the model-tree. The fitted variables are always arrays with 12 entries, one for each permutation.

6 Results

The Kinematic Likelihood Fitter (KLFitter) is applied to all input files with different jet energy scales (JES) from 0.6 to 1.4. An analysis of the energy resolution, the reconstructed top mass and the reconstruction efficiency is performed in order to study the impact of the JES on the top reconstruction with the kinematic fit. The JES is estimated in the fitting procedure. In a second step, the JES estimated in the sample and its uncertainty are used as an input to enhance the quality of the top reconstruction in a subsequent fit.

As an example, the energy resolution of the hadronic b-quark is plotted for every JES in the three steps: before the fit, after the first and after the second fit.

Throughout all the plots of this analysis, the colour code for the different jet energy scales is chosen such that $JES = 1$ is indicated as a solid, red line. Two jet energy scales with the same difference to unity (e.g. 0.9 and 1.1) are drawn in the same colour. $JES < 1$ have dotted lines, $JES > 1$ by contrast have dashed lines.

6.1 Energy Resolution before the Fit

Before the generated events are fitted, the energy resolution of the original (smeared) sample is analysed in order to get reference plots for later comparisons (see chapter 6.5). All energy resolutions of the four jets and the electron are shown in fig. (A.1). The p_z resolution of the neutrino can only be analysed after the fit as $p_z(\nu)$ cannot be measured. The energy resolution is defined as $\frac{E_{true}-E_m}{\sqrt{E_{true}}}$, where E_m is the measured (smeared) energy and E_{true} the true, unsmeared energy.

The energy resolutions of b_{had} are shown as one example in fig. (6.1). They differ substantially from each other for different jet energy scales. For $JES \neq 1$ the distributions are asymmetric because the energy difference is divided by the square root of the true energy. Exclusively for $JES = 1$ the resolution is symmetrically distributed around zero. This means $\langle E_m \rangle \approx \langle E_{true} \rangle$. The root mean squared

6 Results

(RMS) of the distribution $RMS/\sqrt{\text{GeV}} = 0.496 \pm 0.004$ is the smallest here compared to the other jet energy scales. It is consistent with the smearing parameter $a_{\text{had}} = 50\%$ within the error. The mean of each resolution distribution is shifted towards larger values for decreasing jet energy scales. Accordingly, the measured energies are smaller than the true ones due to the $JES < 1$. Increasing the jet energy scales with $JES > 1$ leads to $E_m > E_{\text{true}}$ resulting in a negative mean of the energy resolution. The widths of the distributions broaden for increasing $|JES - 1|$, symmetrically for $JES < 1$ and $JES > 1$. The mean and RMS of the energy resolution of b_{had} are determined for each JES and compared (in $\sqrt{\text{GeV}}$) in table (6.1). The mean ranges from -4.379 (JES=1.4) to $+4.401$ (JES=0.6), the RMS from 0.496 (JES=1.0) to 1.723 (JES=1.4).

On the other hand, the electron energy has not been scaled and is therefore approximately independent of the JES.

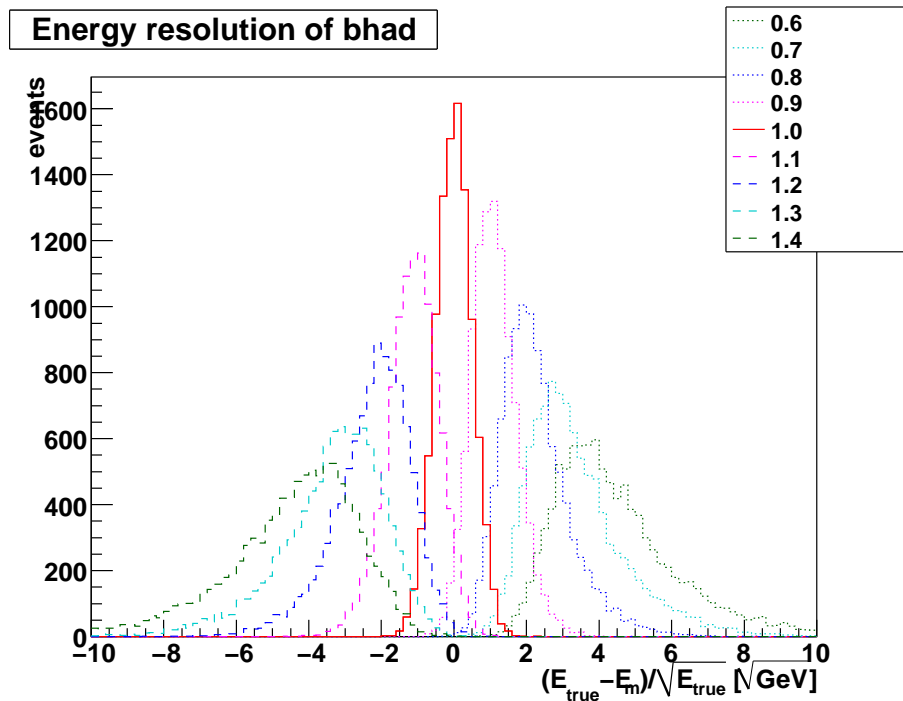


Figure 6.1: Energy resolution of the hadronic b-quark before the kinematic fit: Both the mean and the width depend strongly on the JES. The different jet energy scales are represented by the colours as explained in the legend.

Table 6.1: Mean and RMS of the energy resolution of the hadronic b-quark (smeared, unfitted).

JES	Mean [$\sqrt{\text{GeV}}$]	RMS [$\sqrt{\text{GeV}}$]
0.6	+4.401(16)	1.620(11)
0.7	+3.348(13)	1.342(9)
0.8	+2.246(9)	0.956(7)
0.9	+1.112(6)	0.627(4)
1.0	+0.004(5)	0.496(4)
1.1	-1.130(7)	0.708(5)
1.2	-2.241(11)	1.055(7)
1.3	-3.354(14)	1.445(10)
1.4	-4.379(17)	1.723(12)

6.2 Results of the First Fit

The KLfitter is applied to the smeared samples using the two different mass constraints, i.e., equal top and antitop masses (EM) or a Breit-Wigner (BW) function for both top masses centered at 170 GeV. The results for the energy resolution, the reconstruction efficiency and m_t are only preliminary because a second fit will be performed afterwards.

Energy resolution After the input samples are fitted, the energy resolution can be compared to the energy resolution before the fit. Fig. (A.2) and (A.3) show $\frac{\Delta E}{\sqrt{E_{true}}}$ for the b- and light quarks for both constraints. Paradigmatically, the energy resolution of the hadronic b-quarks is analysed for both constraints (fig. 6.2). The mean and the width are extracted and summarized in table (6.2).

These results constitute a significant improvement compared to the smeared, unfitted energies. Firstly, all distributions are centered around ~ 0 which means that the estimator for the energy is hardly biased. Secondly, the widths (in [$\sqrt{\text{GeV}}$]) were reduced to a range of 0.497 – 0.541 for BW and to a range of 0.820 – 0.918 for EM. So, the maximum relative improvement $\frac{\text{RMS}_{\text{meas}} - \text{RMS}_{\text{fit}}}{\text{RMS}_{\text{meas}}}$ is 70.37% for BW with JES=1.4 and 48.02% for EM with JES=0.6.

In conclusion, it can be stated that in case of the BW constraint the width depends on the JES only to a minor degree, whereas it varies more for the equal mass constraint. The widths are reduced for both constraints, but a better resolution is achieved by the BW constraint for both top quarks due to the additional constraint. An overview

6 Results

over the achievements of each fit is given in fig. (6.12).

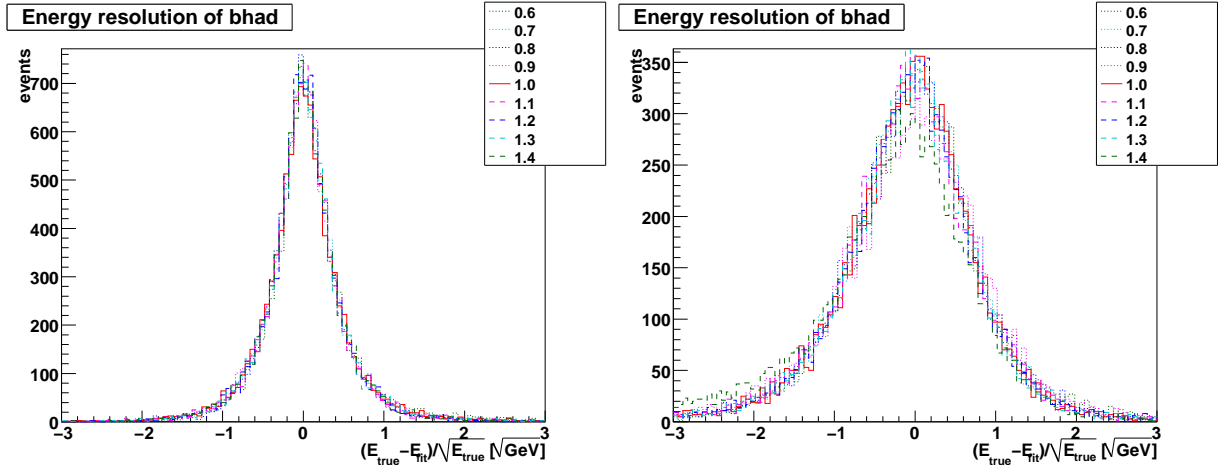


Figure 6.2: Energy resolution of the hadronic b-quark after the first fit with the BW (left) and EM constraint (right) for the best combination.

Table 6.2: Mean and RMS of the energy resolution of the hadronic b-quark for the BW and EM constraint.

JES	BW Mean [$\sqrt{\text{GeV}}$]	BW RMS [$\sqrt{\text{GeV}}$]	EM Mean [$\sqrt{\text{GeV}}$]	EM RMS [$\sqrt{\text{GeV}}$]
0.6	0.0655(54)	0.5414(39)	-0.0086(85)	0.8421(60)
0.7	0.0242(49)	0.4971(35)	-0.0490(83)	0.8203(59)
0.8	0.0176(51)	0.5093(36)	-0.0459(83)	0.8198(59)
0.9	0.0108(51)	0.5066(36)	-0.0447(91)	0.8901(64)
1.0	0.0108(51)	0.5058(36)	-0.0682(83)	0.8202(59)
1.1	0.0073(51)	0.5172(37)	-0.0779(84)	0.8287(60)
1.2	0.0104(50)	0.4994(35)	-0.0724(84)	0.8246(59)
1.3	0.0125(51)	0.5066(36)	-0.0811(84)	0.8228(60)
1.4	-0.0005(51)	0.5106(36)	-0.2172(96)	0.9176(68)

Reconstruction Efficiency The reconstruction efficiency is defined as the ratio between correctly identified objects to all events. One can either count the frequency that all the four jets are assigned correctly to the four quarks. Or a specific particle is chosen. In the following, the efficiencies for a completely correct reconstruction (true combination), the reconstruction of the hadronic W-boson and the two b-jets are considered. Moreover, the separation of light and b-jets is analysed.

The two mass constraints are differently efficient in identifying the true combination. The first bins of fig. (6.2, left) and (6.2, right), respectively, display how often the best combination agrees with the true combination. It emerges that the true combination is found in 80% of the events by the BW constraint and in 50% of the events by the EM constraint. In the former case there is one more constraint which can explain this difference.

If the kinematic fit is not taken into account, the probability P for the correct identification of a jet can be gained from pure statistics¹. Only in one of the twelve cases all the four jets are correctly identified (true combination), so $P(\text{all correct}) = \frac{1}{12} \approx 8.33\%$.

But there are two possibilities to reconstruct the hadronic W-boson correctly because interchanging the two b-quarks does not alter the W-momentum $p_W = p_{q1} + p_{q2}$. This implies $P(W_{had} \text{ correct}) = \frac{2}{12} \approx 16.66\%$.

For the right labelling of the hadronic (leptonic) b-quark it is still possible to commute the remaining three jets among themselves. Thus, $\frac{3!}{2} = 3$ permutations result in a right assignment for the hadronic (leptonic) b-quark with a probability of $P(b_{lep/had} \text{ correct}) = \frac{3}{12} = 25\%$ each.

For example, for tests of b-tagging algorithms, it is essential to work out how reliably the reconstruction procedure can distinguish between light and b-jets. Let $P(b \text{ tag} | \text{truth } b)$ be the probability to tag a true b-jet as a b-jet. Here, the leptonic b-jet may still be labelled as the hadronic one and vice versa. With the knowledge that two of the four jets are b-jets, the probability is $P(b \text{ tag} | \text{truth } b) = \frac{2}{4} = 50\%$ from a combinatorial point of view. If a true b-jet is omitted to be labelled as a b-jet, this is called 'type I error' (discarding a true event) in the context of hypothesis testing. The error probability here is

$$\alpha = P(\text{type I error}) = 1 - P(b \text{ tag} | \text{truth } b) = 50\%.$$

The second question of interest is the probability to designate a jet as a b-jet provided that it is in fact a jet from a light quark. This acceptance of a wrong event is called a 'type II error' with a probability of

$$\beta = P(\text{type II error}) = P(b \text{ tag} | \text{light quark}) = 50\%.$$

¹As remarked in chapter (5.2) the combinations with interchanged light quarks are counted only once.

6 Results

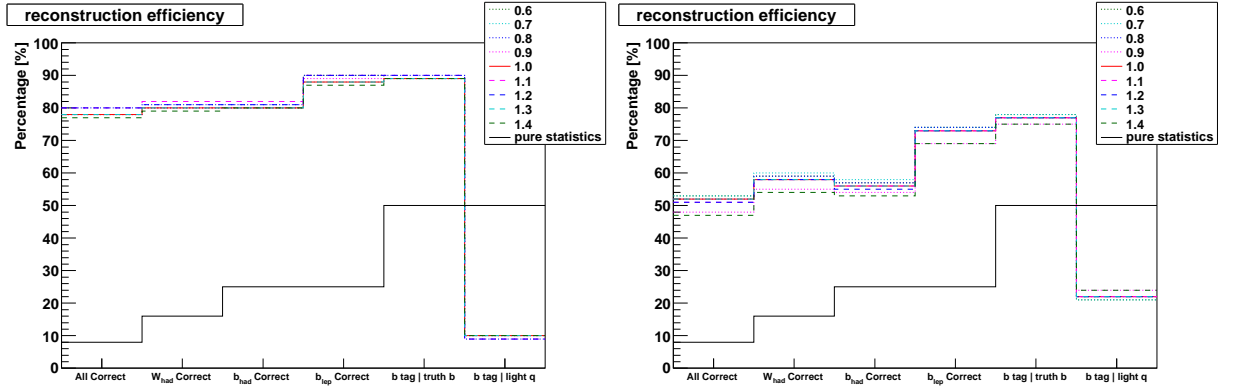


Figure 6.3: Reconstruction of all jets W_{had} , both b-jets and b-tagging efficiencies for BW (left) and EM (right). Percentages from fit (coloured) are compared to pure statistics (black).

These probabilities from pure statistics are indicated in fig. (6.2, left) and (6.2, right) with a black line. But the reconstruction efficiencies from the kinematic fit are distinctly above the combinatorial ones. For instance, $P(all\ correct)$ is augmented from $\sim 8\%$ to $\sim 80\%$ ($\sim 50\%$) in for BW (EM).

The leptonic b-jet is correctly identified at a percentage of $\sim 88\%$ ($\sim 70\%$) instead of 25%. The identification of b_{lep} succeeds better to $\sim 10\%$ ($\sim 20\%$) compared to b_{had} . This results from the separation of the top-/ antitop hemispheres using a top mass constraint. The b_{lep} is the only jet in the leptonic hemisphere, whereas there are also the two light jets on the hadronic site in addition to b_{had} .

While the $P(all\ correct) \approx P(W_{had}\ correct)$ in the BW case, there is a difference of about 10% between the reconstruction efficiencies of all jets and the hadronic W-boson for the EM constraint. Here, the two b-jets are mixed up which is also reflected by the lower efficiencies for b_{had} and b_{lep} .

The b-tagging errors of type I and II are decreased by circa 40% (BW) or 25% (EM) so that truth b-jets are labelled as b-jets with a probability of $\sim 90\%$ (BW) or $\sim 75\%$ (EM) instead of only 50%. This comparison shows how the utilization of kinematic constraints enhances the reconstruction quality.

Contrasting the efficiencies for both constraints, the percentages are higher for the Breit-Wigner constraint on m_t than for EM. It also becomes apparent that the reconstruction efficiency depends on the JES to a greater degree for the equal mass constraint. The reason is again the double constraint of BW for both top quarks.

Top Mass The masses of the leptonic and hadronic top quarks can be calculated from the fitting results using energy and momentum conservation:

$$p_{W_{\text{lep}}} = p_{\nu} + p_l, \quad p_{W_{\text{had}}} = p_{q_{\text{up}}} + p_{q_{\text{down}}} \quad (6.1)$$

$$p_{t_{\text{lep}}} = p_{W_{\text{lep}}} + p_{b_{\text{lep}}}, \quad p_{t_{\text{had}}} = p_{W_{\text{had}}} + p_{b_{\text{had}}} \quad (6.2)$$

$$\Rightarrow m_{t_{\text{lep}}}^2 = p_{t_{\text{lep}}}^2/c^2, \quad m_{t_{\text{had}}}^2 = p_{t_{\text{had}}}^2/c^2 \quad (6.3)$$

The reconstructed top masses shown in fig. (6.4) are those bins with the maximum entry.

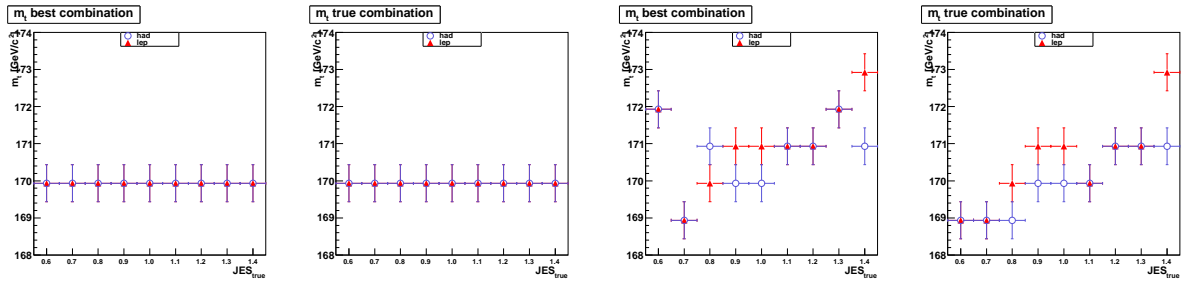


Figure 6.4: Peak top masses after the first fit with BW (two left plots) and EM (two right plots) constraint. The best and true combination are compared. The hadronic and leptonic top are marked differently.

Although the BW constraint cannot be used for a top mass measurement, the top mass dependence on the JES is studied as an approach of a cross-check. The BW constraint uses $m_t = 170 \text{ GeV}/c^2$ as a peak of the distribution. As expected, the BW constraint returns the input top mass of $m_t = 170 \text{ GeV}/c^2$ independently of the JES. But the mass is not fixed by the EM constraint. Therefore, it varies in the range $m_t^{\text{EM}}[\text{GeV}/c^2] \in [169, 173]$. Wrong combinatorics cause too large masses in some cases in the best permutation. Besides, it can be observed that the leptonic top tends to have a larger reconstructed mass than the hadronic.

Even though the reconstructed peak top masses are close to $170 \text{ GeV}/c^2$, no conclusion about the mass distribution can be drawn from fig. (6.2). In fact, it is a sharp peak for BW, but for EM it is a broad distribution with an asymmetric tail to larger masses. For this reason, an accurate peak mass is not a sufficient criterion for a "good" mass estimation.

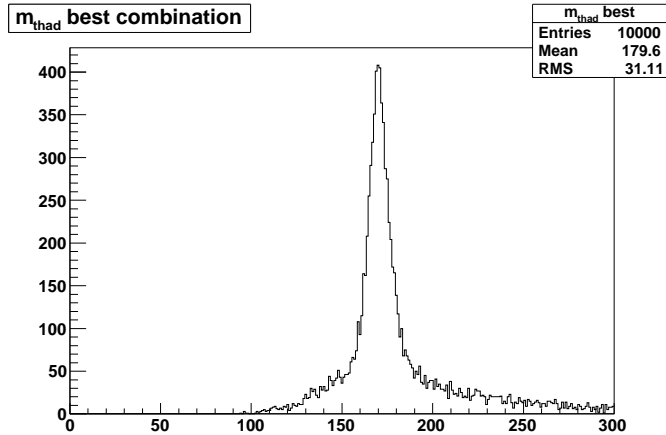


Figure 6.5: Distribution of $m_{t_{\text{had}}}$ for JES=1.0 with EM after the first fit.

Thus, analysing the mean of the mass distributions instead of the maximum bins leads to masses $> 170 \text{ GeV}/c^2$. The asymmetric EM masses are likely to result from asymmetric JES distributions (fig. A.5). Tails with too low estimated jet energy scales are correlated with tails of too large masses and vice versa. However, one has to keep in mind that this was only the first step of the fitting procedure. The development of the mass distributions will be examined in chapter (6.4.2).

6.3 Determination of the Global Jet Energy Scale

For each input file the true JES is known which was used in the MC simulation. But the kinematic fit treats the JES as an additional free parameter. Consequently, the fitted JES can differ from the true one. In order to reduce the uncertainties from the JES, a calibration of the JES is necessary. For a given JES_{true} the distribution of JES_{est} is plotted. This is done for all JES_{true} in the best and true combination with the BW and EM constraint on m_t . These plots can be found in appendix A (fig. A.4 and A.5), the different jet energy scales are combined in summary plots (fig. 6.3). In the following a procedure is described how to extract the mean and error of JES_{est} and to test if there is a linear dependency of JES_{est} on JES_{true} .

The various estimated jet energy scales JES_{est} can be fitted by a Gaussian distributions in the region around the peak only because the tails are clearly non-Gaussian. Therefore, the range for the fit is reduced to a $\pm 10\%$ neighbourhood of the bin with the maximal content, bin_{peak} . The corresponding JES is $\text{JES}_{\text{peak}} = \text{JES}(\text{bin}_{\text{peak}})$

6.3 Determination of the Global Jet Energy Scale

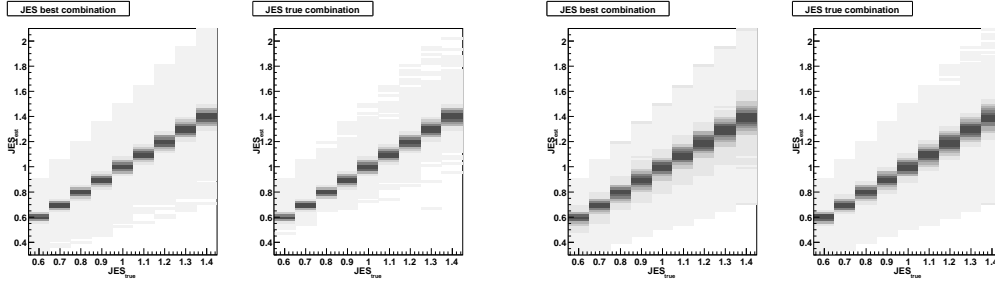


Figure 6.6: Estimated versus true JES for the BW (two plots left) and EM constraint (two plots right) in the best (each left) and true (each right) combination.

The error on the peak JES is half of the bin width. Subsequently, JES_{est} is fitted in the range $[0.9 \cdot JES_{peak}, 1.1 \cdot JES_{peak}]$, mean and σ are extracted from the fit.

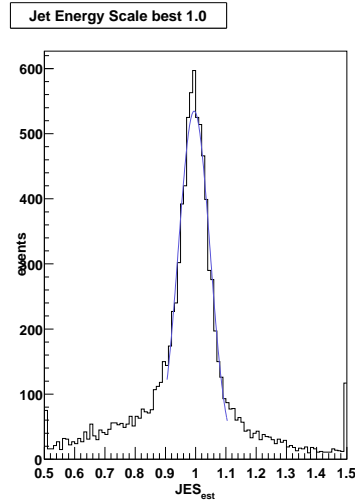


Figure 6.7: Gauss fit in the reduced range for JES=1.0 with EM constraint.

While the JES distributions agree well with a Gauss function for the BW constraint (fig. A.4), in case of the equal mass condition, however, the necessity of limiting the fitting range becomes evident (fig. A.5).

Then the peak JES of the histogram as well as the mean of the Gauss fit are fitted according to

$$JES_{fit}(JES_{true}) = p_1 \cdot JES_{true} + p_0$$

Fig. (6.3) show these straight line fits as calibration curves for the BW and EM constraint in the best and true combination. A slope of $p_1 = 1$ and an intercept

6 Results

of $p_0 = 0$ are expected. Besides, the residuals $\frac{\Delta \text{JES}}{\sigma}$ are computed, where $\Delta \text{JES} = \text{JES}_{\text{est}} - \text{JES}_{\text{fit}}$ quantifies the deviation of the estimated points from the linear fit and σ is the error on JES_{est} . Since there are both positive and negative residuals, no bias towards lower or higher jet energy scales is perceived. So the fit appears to be balanced.

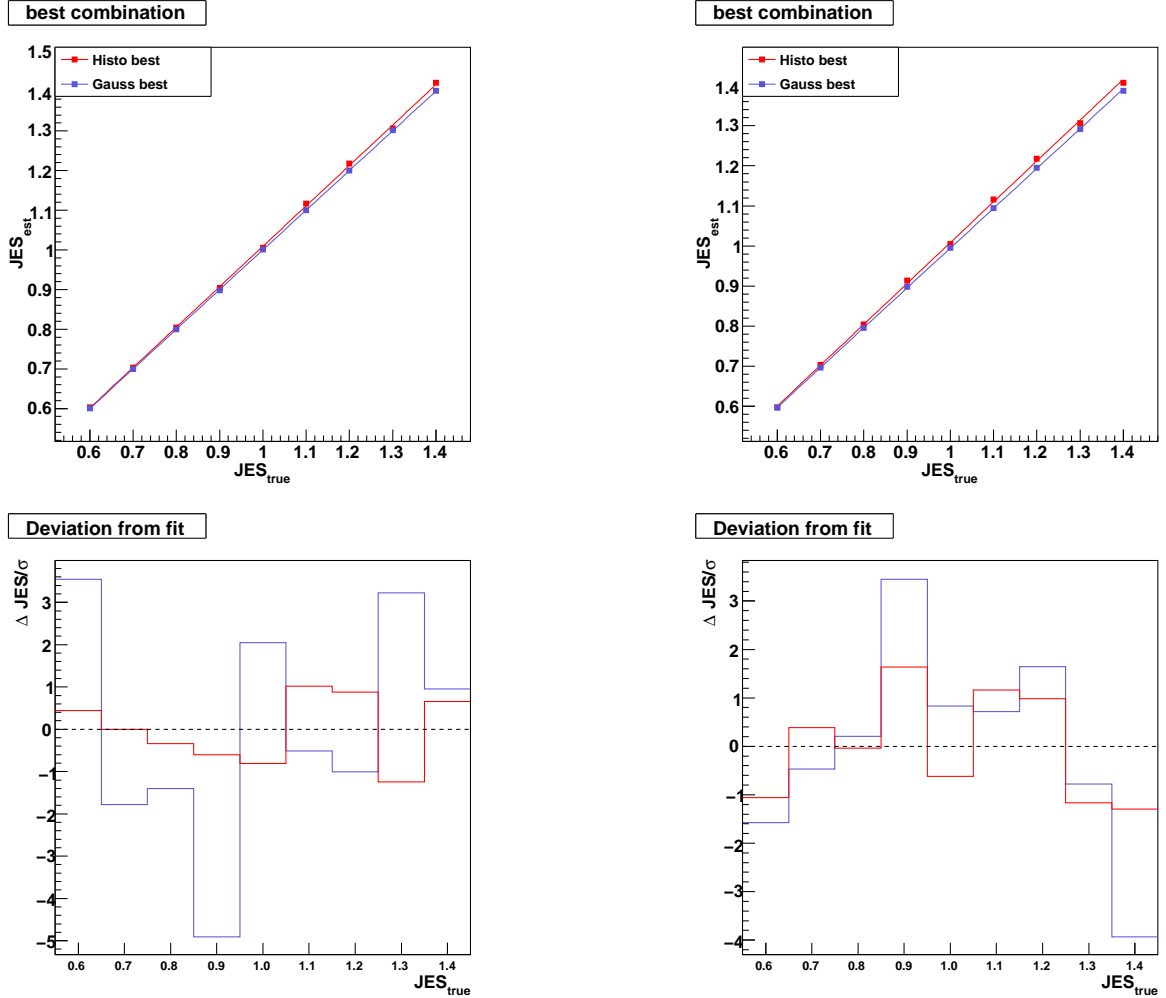


Figure 6.8: Calibration curve of JES_{est} versus JES_{true} for BW (left) and EM (right). The estimated JES represents the best permutation. Points of "Histo best" are the mean values of the histograms; "Gauss best" denotes the mean values of the Gaussian fit. The residuals (below) display the deviation of a point from the fit, weighted with its error.

Table 6.3: Fit parameters of the straight lines: slope and intercept for Gaussian fit and histogram points, with BW and EM constraint.

	BW p_1	BW p_0	EM p_1	EM p_0
Gauss best	1.00049	-0.00049	0.99405	0.00038
Gauss true	0.99986	0.00013	0.99393	0.00244
Histo best	1.01842	-0.00937	1.01985	-0.01173
Histo true	1.00234	0.00196	0.99097	0.00633

Table (6.3) summarizes the slopes and intercepts of the linear fits. The intercepts turn out to be approximately zero so that no systematic bias of the JES estimator needs to be considered. The slopes are approximately 1, but with different large deviations. The straight lines referring to the histogram data are systematically steeper due to small asymmetric tails towards higher jet energy scales which are cut off in the Gauss fit. The slope for a BW constraint is close to unity while the equal mass slope differs more due to broader distributions and asymmetric tails (see fig. A.5). Nevertheless, the straight lines confirm the linear relation². The deviation discussed here are at or below the percent level and it is only the first fit.

6.4 Second Fit

With the insights from the extraction of the JES, the KLFFitter runs a second time over the MC sample using the JES estimated from the sample as an *a priori* probability for the renewed estimation. The goal is to improve the variables of physical interest, to reduce the influence of the JES on them and to cross-check the consistency of the KLFFitter.

6.4.1 a priori Probabilities

Let $p(a|x)$ be the probability that a is true provided that x is true and $p_0(a)$ the a priori probability for a . *Bayes' Theorem* gives an important relation between conditional and a priori probabilities [30]:

$$p(a|x) = p(x|a) \cdot \frac{p_0(a)}{p(x)} \quad (6.4)$$

²Errors of the fit parameters can be found in fig. (A.6) and (A.7).

6 Results

With the partition of the set of events into disjoint events $\{a_i\}_{i=1,\dots,N}$ this is generalized to

$$p(a_i|x) = \frac{p(x|a_i)p_0(a)}{p(x)} = \frac{p(x|a_i)p_0(a)}{\sum_{j=1}^N p(x|a_j)p(a_j)} \quad \text{with} \quad \sum_{i=1}^N p(a_i|x) = 1$$

and in a continuous set of events the normalization is an integral [29]:

$$\int d\vec{a} p(\vec{a}|\vec{x}) = \int d\vec{a} \frac{p(\vec{x}|\vec{a})p_0(\vec{a})}{\int d\vec{a}' p(\vec{x}|\vec{a}')p(\vec{a}')} = 1 \quad (6.5)$$

If no specific information is given, the a priori probability $p_0(\vec{a})$ is uniformly distributed and constant so that it cancels out in eq. (6.5). In the first run the KLfitter does not get any information about the JES, the a priori probabilities are automatically set to 1. But in the second fit the mean and σ of each JES is used as parameters for a normalized Gauss function which overwrites the constant a priori probability.

6.4.2 Results of the Second Fit

Energy Resolution

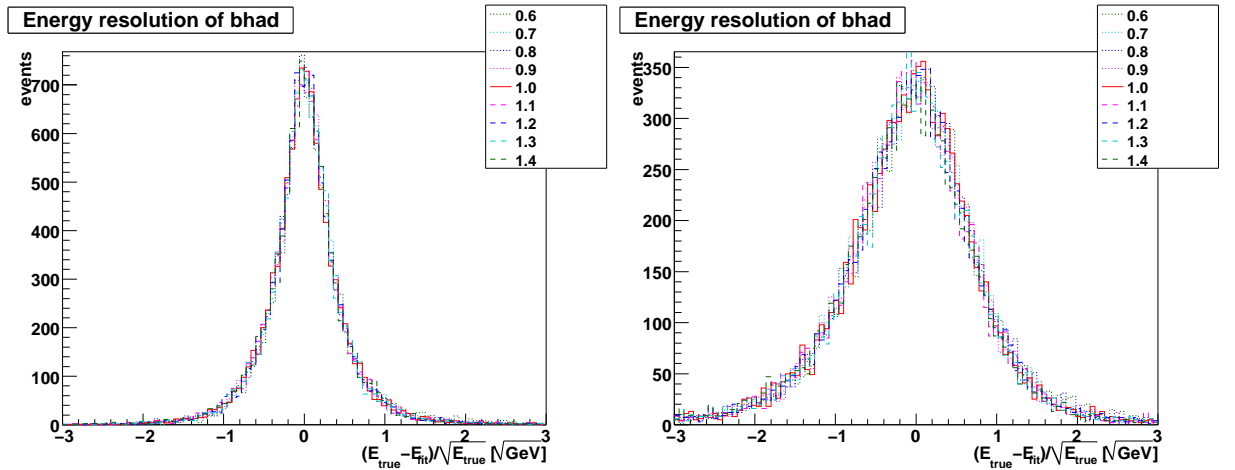


Figure 6.9: Energy resolution of the hadronic b-quark after the calibration with the BW (left) and EM constraint (right) for the best combination.

As observed in chapter 6.2, the energy resolutions are centered around zero, the widths are nearly constant for all jet energy scales and they are better for the BW constraint than for EM. The improvement of the resolution after the calibration compared to the first fit is smaller, but nevertheless appreciable: The RMS is changed for EM by 9.82% from $0.85 \sqrt{\text{GeV}}$ to $0.775 \sqrt{\text{GeV}}$. For the BW constraint the change from $0.5 \sqrt{\text{GeV}}$ to $0.4 \sqrt{\text{GeV}}$ means even a relative improvement of 20%. Accordingly, the second fit with the BW constraint causes in fact falling below the initial resolution of $0.5 \sqrt{\text{GeV}}$ from the Gaussian smearing. The additional pieces of information from the constraints prevail the fitting uncertainties so that the energy resolution obtained from the fit is better than in the input samples.

Reconstruction Efficiency The reconstruction efficiencies are calculated anew as described in chapter (6.2). They are shown in fig. (6.10).

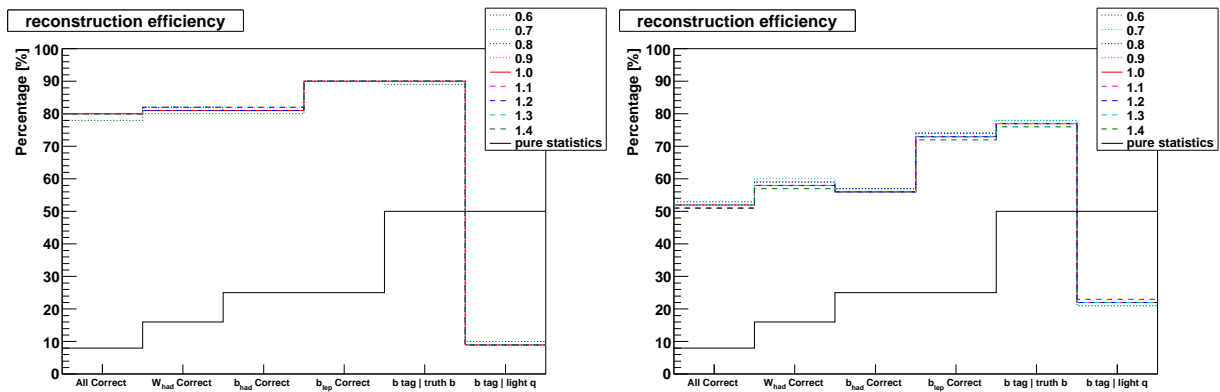


Figure 6.10: Reconstruction efficiencies for BW (left) and EM (right) after the second fit taking the a priori probabilities into account.

Especially in case of the equal mass constraint the a priori probabilities result in a notable improvement of the efficiencies. For example, the difference between the lowest and highest reconstruction efficiency depending on the JES for the leptonic b-jet is 6% before the calibration (fig. 6.2) and afterwards it is reduced to 2%. The efficiencies for BW are nearly independent of the JES after the calibration. As seen before, the BW constraint yields higher absolute efficiencies than EM, but the effect of the second fit is less compared to EM.

Top Mass Again, the top mass is analysed as it can be seen in fig. (6.11). On the one hand, in comparison to fig. (6.4), the peak masses corresponding to the maximum bin change little compared to the first fit. The BW constraint returns the true top mass of $170 \text{ GeV}/c^2$ in both steps of the fitting procedure as a sharp peak. This indicates that the cross-check worked well. On the other hand, the range of the top masses (in GeV/c^2) with the EM constraint is reduced from $[169, 173]$ to $[169, 172]$. The top and antitop masses are similar, but not always equal due to the top width and a weaker constraint than BW.

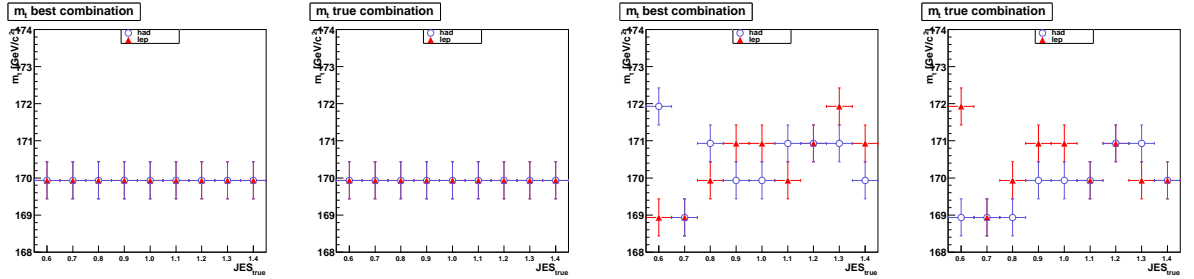


Figure 6.11: Reconstructed peak top masses after the second fit with BW (two plots left) and EM (two plots right).

The development of the widths of the mass distribution for the EM constraint might also be interesting. The RMS of the hadronic top masses after the first is compared to the second fit in table (6.4). After both steps of the fitting procedure the RMS increases with the JES. Although no systematic improvement of the RMS is achieved by the second fit, the range (in GeV/c^2) in which the RMS can vary for different jet energy scales is reduced from $[29.57, 33.39]$ to $[29.64, 31.64]$.

Table 6.4: Width (RMS) of the hadronic top mass after the first and second fit for the different jest energy scales.

RMS	0.6	0.7	0.8	0.9	1.0	1.1	1.2	1.3	1.4
1st [$\frac{\text{GeV}}{c^2}$]	29.57	30.06	30.72	31.56	31.11	31.15	31.20	31.41	33.39
2nd [$\frac{\text{GeV}}{c^2}$]	29.64	30.19	30.63	31.10	31.04	31.18	31.27	31.29	31.64

6.5 Development of the JES Dependence

Energy resolution Fig. (6.12) shows how the width (RMS) and the mean of the energy resolution of b_{had} change in the two different constraints and steps of fitting.

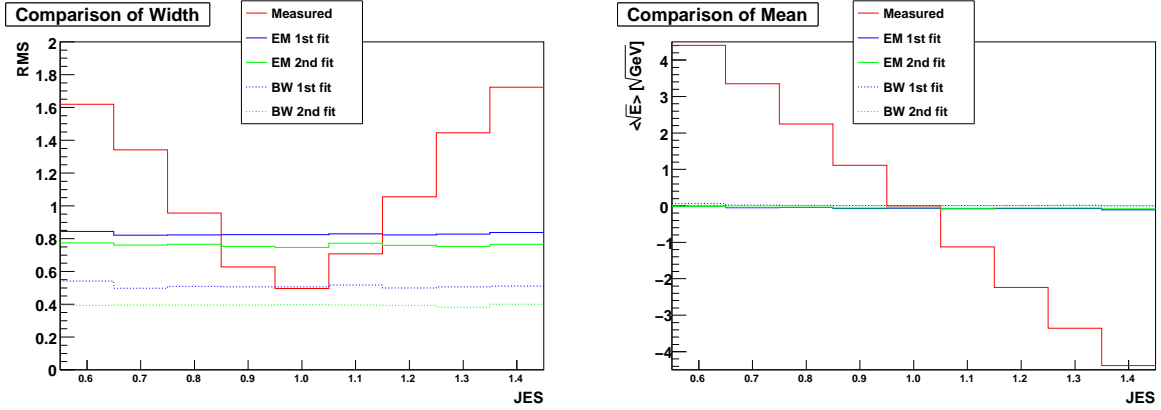


Figure 6.12: Improvement of the width (left) and mean (right) of the energy resolution of the hadronic b using different constraint and fitting twice.

The RMS and mean of the smeared energy resolutions depend strongly on the JES. The first fit achieves that they become nearly JES-independent. Additionally, it leads to a narrowing of the energy distributions which can be seen with the aid of the smaller widths in fig. (6.12, left). But it also turns out that in the JES range of $[0.9, 1.1]$ the resolution is worsened by the uncertainties of the fit with the EM constraint only. The right plot shows an improvement of the accuracy $E_m \approx E_{fit}$ as the mean becomes JES-independent and close to zero. The second fit is not able to improve the resolution as much as the first fit. Nevertheless there is a notable change which gains in case of the BW constraint an energy resolution after the second fit which is better than the resolution of the unfitted, smeared energies.

Reconstruction efficiency Table (6.5) summarizes the narrowing of the efficiency range on the example of *all correct* and b_{lep} . The lower limit of the efficiency range is the percentage of the JES with the worst efficiency, the upper limit belongs to the JES with the highest percentage. The efficiencies are a little improved or constant for a given JES so that the worst results are cut off by the second fit.

Table 6.5: Overview of the improvement of the reconstruction efficiencies for both constraints after the calibration

Efficiency	1st fit	2nd fit
BW all	77 – 80%	78 – 80%
BW blep	86 – 90%	90%
EM all	47 – 53%	51 – 53%
EM blep	68 – 73%	71 – 73%

Top mass The EM constraint reconstructs a too large mean due to the asymmetric tails of the broad distribution. Yet, the second fit leads to considerably better results. But the width of the distribution still depends on the JES. Concerning the peak mass, the hadronic and leptonic top mass are similar, but not equal. The BW constraint succeeds in finding the correct top peak mass directly in the first fit and the correct mean after the second fit – independently of the JES. This cross-check confirms the reconstruction.

7 Conclusion

Finally, the methods and results of this thesis are summarized and further studies are proposed in an outlook.

7.1 Summary

In the framework of this bachelor's thesis the impact of the jet energy scale (JES) on the reconstruction of top-antitop-pairs in the semileptonic decay channel with one electron and four jets was studied in the context of a kinematic fit based on the Maximum Likelihood principle.

The JES was added to the KL Fitter as a new parameter which can be varied independently. The kinematic fit was then applied to different Monte Carlo samples with jet energies ranging from 0.6 to 1.4 in steps of $\Delta\text{JES} = 0.1$. As a toy model, the detector response was assumed to be $\frac{50\%}{\sqrt{E}}$ for hadrons and $\frac{10\%}{\sqrt{E}}$ for electrons. The reconstructed top mass, the energy resolution and the reconstruction efficiencies were determined. The fitted events were compared to the truth MC samples and the smeared ("measured") values.

The conservation of energy and momentum at each decay vertex was taken into account in the Likelihood as kinematic constraints. These were a Breit-Wigner (BW) function for a given mass of the W-boson $m_W = 80.4 \text{ GeV}/c^2$ plus either the requirement of an equal mass (EM) of the top and antitop quark or a Breit-Wigner function for both top quarks centered at $m_t = 170 \text{ GeV}/c^2$. Though introducing a new parameter increases the uncertainties of the fit, the knowledge of the topology of each vertex led to an improvement of the results. After the first fit, the energy resolution was achieved to be distributed around zero for all jet energy scales – unlike before. Additionally, the maximal relative reduction of the widths ranged from $\sim 48\%$ for EM to $\sim 70\%$ for BW.

Subsequently, the estimated JES was extracted from the first fit. Considering these

7 Conclusion

results as a new a priori probability for the estimation of the JES, the fit was performed again. This procedure led to an improvement of the reconstruction efficiency by 4% and to a narrowing of the top mass distribution of up to 5.5%. The second fit improved the energy resolution by 9.8% for EM and 20% for BW which yielded a better resolution than the smeared, unfitted energies.

On the one hand, better absolute results were gained with the BW constraint, but on the other hand, the relative effect of the second fit was larger with the requirement of equal top masses. In general, the influence of the JES on the analysed variables was reduced by the kinematic fit.

7.2 Outlook

Besides studying the effects of a global free jet energy scale parameter in the KLFilter, there are more options for investigations in this context. First of all, a second jet energy scale could be introduced if the BW constraint is applied. As shown in chapter (5.2), an additional fit parameter is possible. This would allow to distinguish between a jet energy scale for light and b-jets.

It would also be interesting to repeat these studies with other energy resolutions in the input samples, i.e. with a different width in the Gaussian smearing or with a non-Gaussian energy resolution. In a next step the JES could also be studied in Monte Carlo events including a full simulation of the ATLAS detector.

A First Appendix: Plots

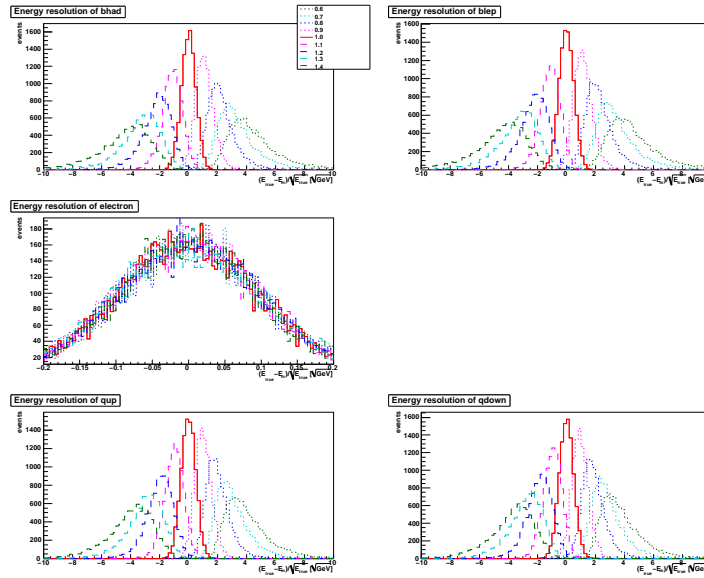


Figure A.1: Resolution of the measured energies before the fit.

A First Appendix: Plots

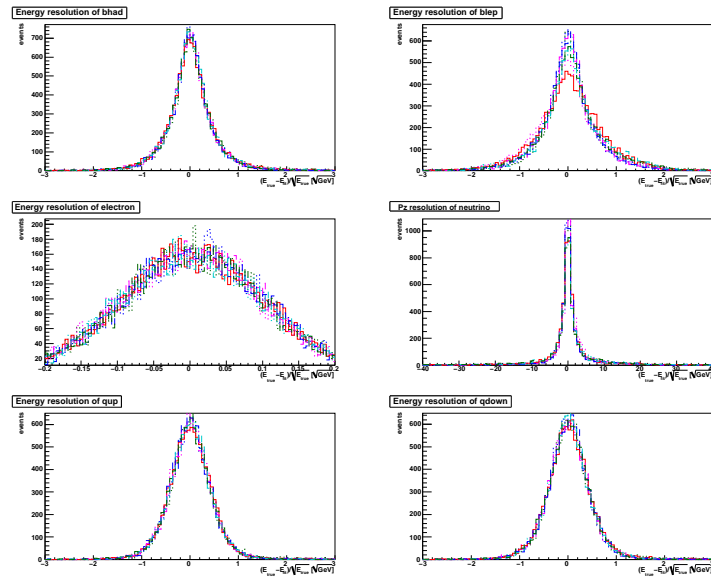


Figure A.2: Energy resolution with BW after the first fit (best combination).

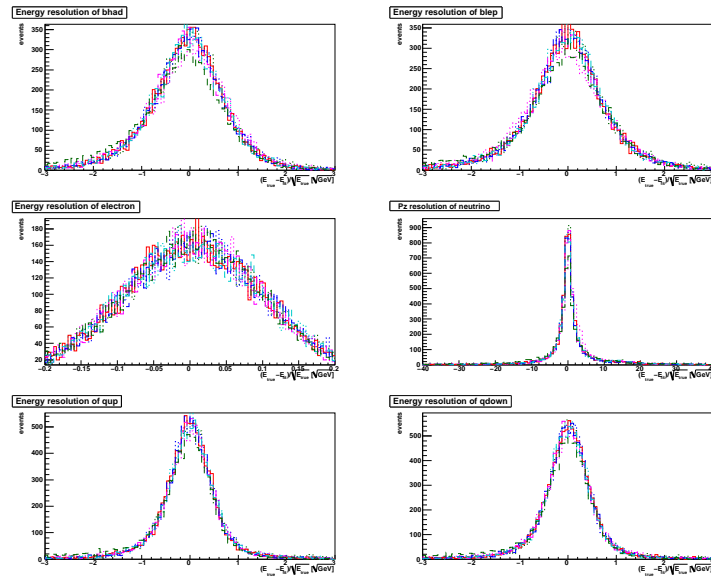


Figure A.3: Energy resolution with EM after the first fit (best combination).

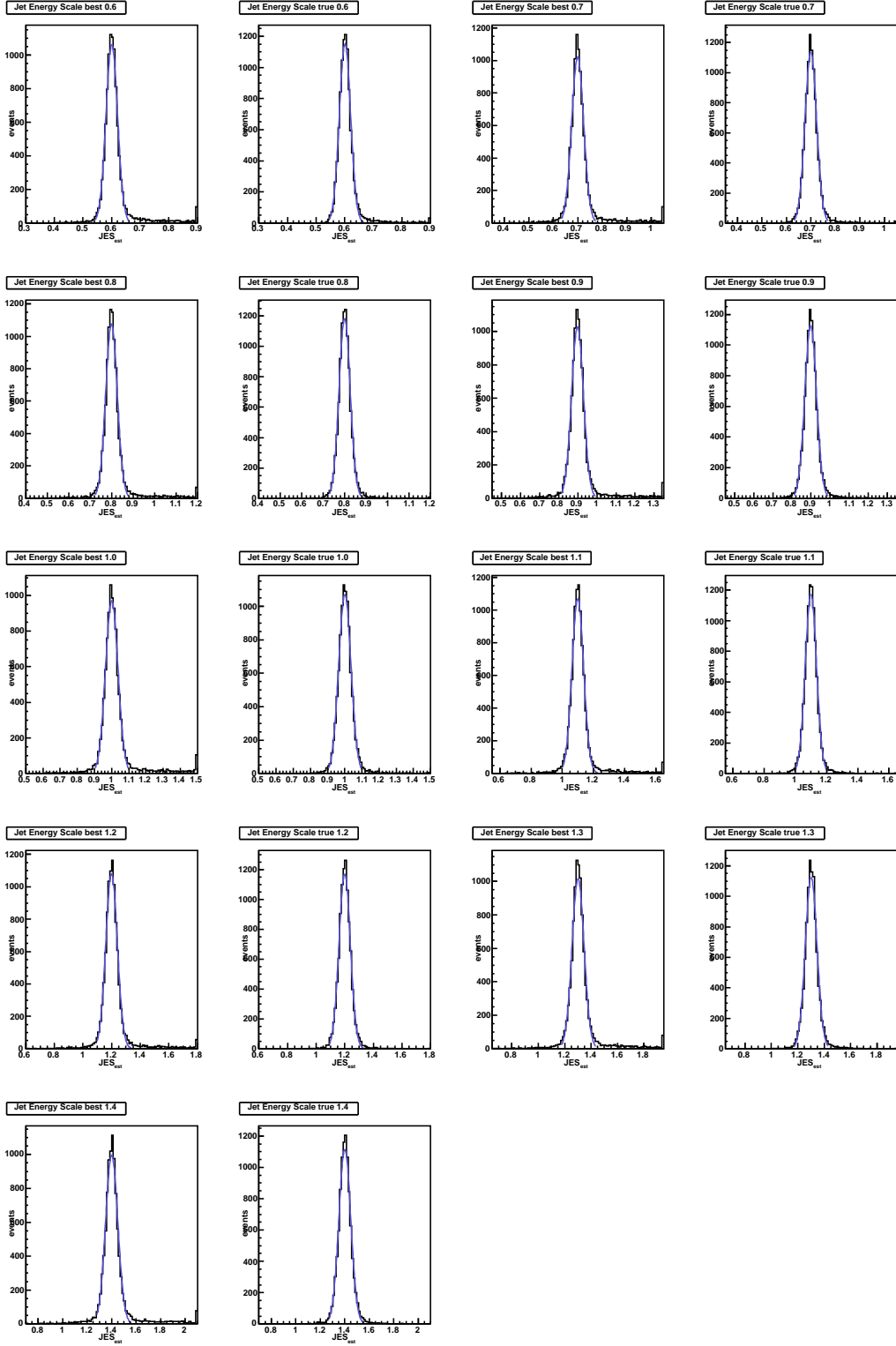


Figure A.4: Distribution of the estimated JES for each true JES with the BW constraint. The best combination (left) is compared to the true one (right).

A First Appendix: Plots

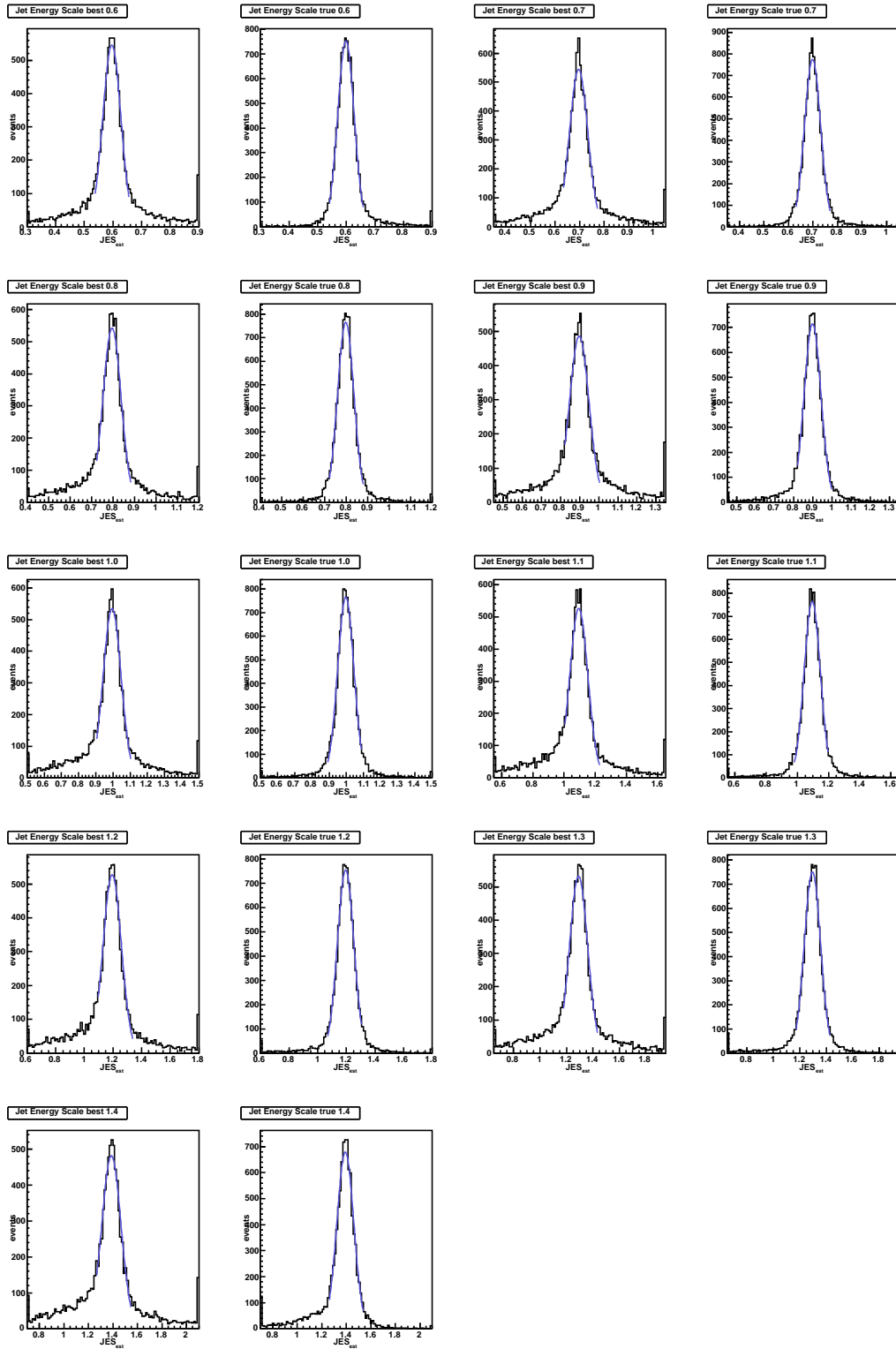


Figure A.5: Distribution of the estimated JES for each true JES with the EM constraint. The best combination (left) is compared to the true one (right).

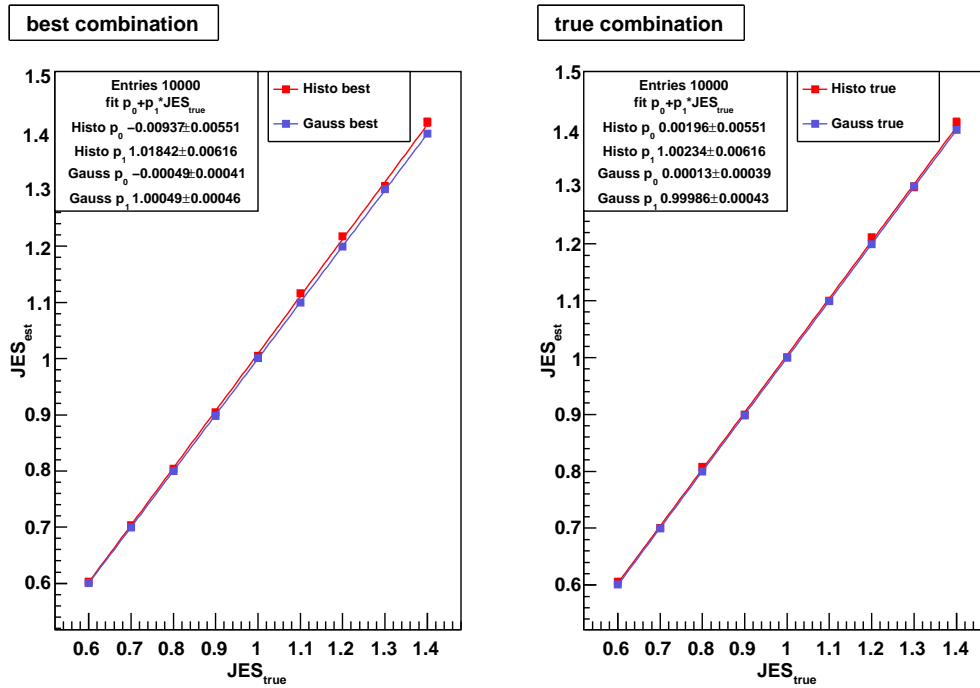


Figure A.6: Calibration curve for BW after the first fit.

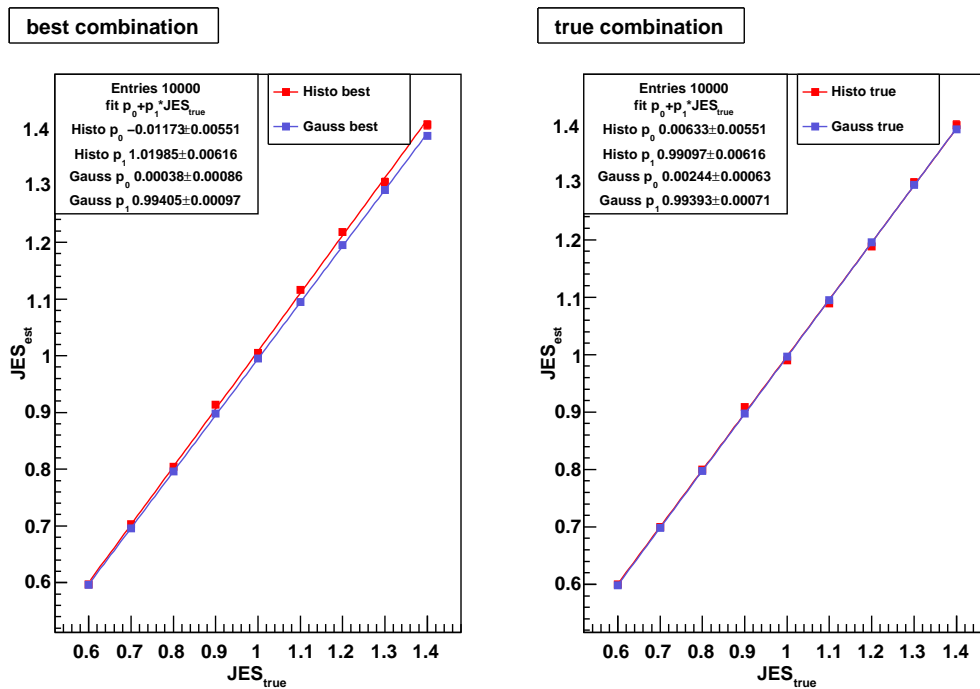


Figure A.7: Calibration curve for EM after the first fit.

A First Appendix: Plots

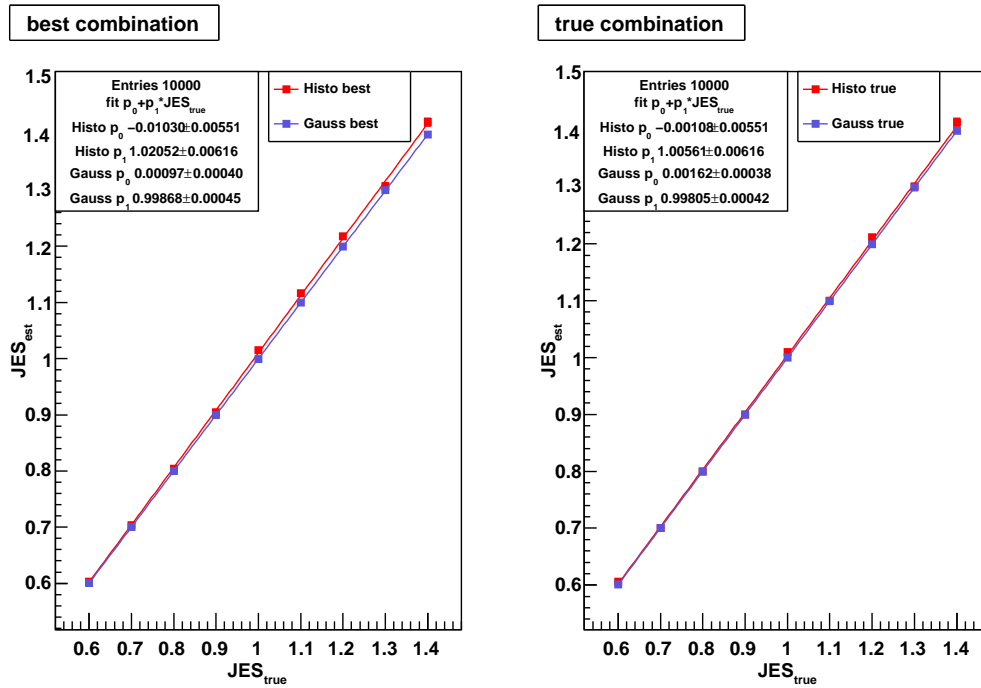


Figure A.8: Calibration curve for BW after the second fit.

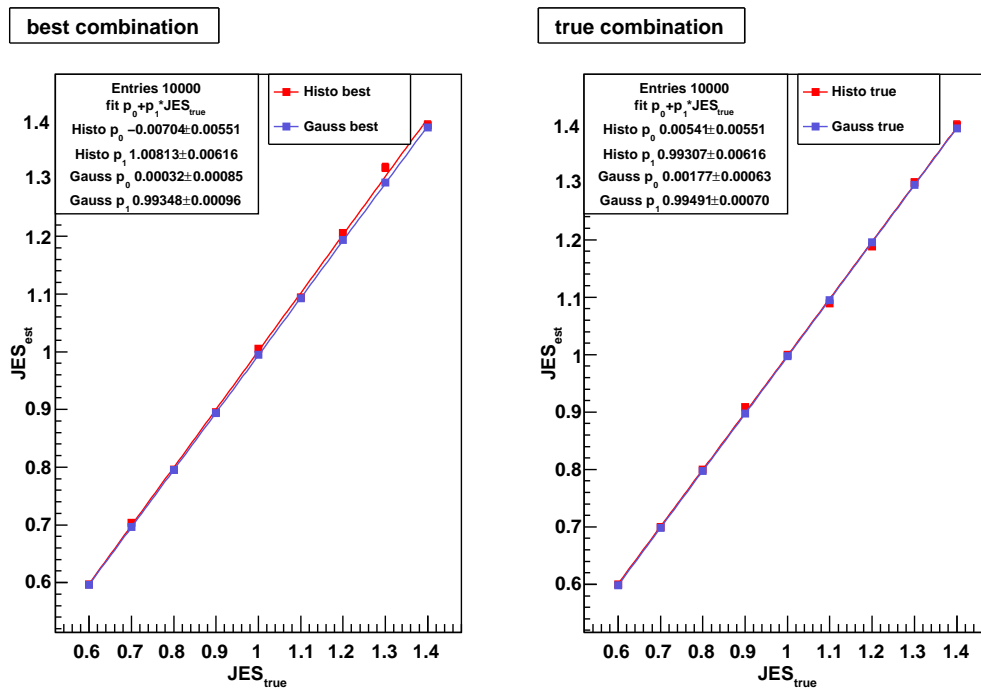


Figure A.9: Calibration curve for EM after the second fit.

Nomenclature

Symbol	Meaning
α	jet energy scale
β	scaling factor of momenta
η	pseudorapidity
θ	polar angle
ϕ	azimuthal angle
σ	width or standard deviation
a	statistical energy resolution parameter
b	systematic energy resolution parameter or bottom quark
BW	Breit-Wigner
c	noise energy resolution parameter
EM	equal mass
E_{fit}	fitted energy
E_m	"measured", i.e. , smeared energy
E_{true}	true energy from MC
I_3	third component of weak isospin
JES	jet energy scale
k	degrees of freedom in the fit
m	mass
MC	Monte Carlo
M	number of fit parameters
N	number of variables
P	number of constraints or probability
Q	electric charge
RMS	root mean squared
SM	Standard Model of Particle Physics
t	top quark

Nomenclature

Bibliography

- [1] D. Griffiths. *Introduction to Elementary Particle Physics*. WILEY-VCH, 2008.
- [2] Tevatron Electroweak Working Group for the CDF and D0 Collaborations. Combination of CDF and D0 Results on the Mass of the Top Quark. *arXiv:0903.2503v1 [hep-ex]*, 2009.
- [3] Particle Data Group. *Particle Physics Booklet*. PDG, 2008.
- [4] M. Kobayashi, T. Maskawa. CP-Violation in the Renormalizable Theory of Weak Interaction. *Progress in Theoretical Physics*, 49(2).
- [5] CDF Collaboration. Observation of Top Quark Production in $\bar{p}p$ Collisions. *Phys.Rev.Lett.* 74:2626-2631, 1995.
- [6] D0 Collaboration. Observation of the Top Quark. *Phys.Rev.Lett.* 74:2632, 1995.
- [7] V. M. Abazov et al. Observation of Single Top-Quark Production. *Phys. Rev. Lett.*, 103:092001, 2009.
- [8] T. Aaltonen et al. First Observation of Electroweak Single Top Quark Production. *Phys. Rev. Lett.*, 103:092002, 2009.
- [9] Bernreuther, W. Top Quark Physics at the LHC. *J.Phys.*, G35:083001, 2008.
- [10] D. Chakraborty, J. Konigsberg, D. Raunwater. Review of Top Quark Physics. 2003.
- [11] T. Liss, A. Quadt. The Top Quark. *PDG*, 2008.
- [12] A. Quadt. Top quark physics at hadron colliders. *Eur. Phys. J.*, C48:835–1000, 2006.
- [13] <http://www.e4.physik.tu-dortmund.de/cgi-bin/twiki/view/ATLAS/TopQuark>.

Bibliography

- [14] Pumplin, J. and others. New generation of parton distributions with uncertainties from global QCD analysis. *JHEP*, 07:012, 2002.
- [15] L. Wolfenstein. Parametrization of the Kobayashi-Maskawa Matrix. *Physics Review Letters*, 51(21), 1983.
- [16] F.J. Gillman, K. Kleinknecht, B. Renk. The Cabbibo-Kobayashi-Maskawa Quark-Mixing Matrix. *PDG*, 2000.
- [17] O. S. Brüning et al. LHC Design Report. *CERN 2004-2003*, 2004.
- [18] ATLAS Technical Report Volume 1. *ATLAS TDR 14, CERN/LHCC 99-14*, 1999.
- [19] <http://public.web.cern.ch/public/en/Research/AccelComplex-en.html>.
- [20] ALICE TDR Technical Design Report. *ATLAS TDR 9 edn., CERN/LHCC 2001-021*, 2001.
- [21] LHCb: Technical Proposal. *CERN/LHCC 98-004*, 1998.
- [22] The CMS Collaboration, G. L. Bayatian et al. CMS Technical Design Report. *CERN/LHCC 2006-004*, 2006.
- [23] J. Aad et al. The ATLAS Experiment at the CERN Large Hadron Collider. *CERN-OPEN-2008-020*, 2008.
- [24] Woudstra, M.J., Linde, F. *Precision of the ATLAS muon spectrometer*. PhD thesis, 2002.
- [25] Maltoni, F., Stelzer, T. MadEvent: Automatic event generation with MadGraph. *JHEP*, 02:027, 2003.
- [26] Alwall, J. and others. MadGraph/MadEvent v4: The New Web Generation. *JHEP*, 09:028, 2007.
- [27] KLFitter – A framework for kinematic fitting using a Likelihood approach. <http://physik2.uni-goettingen.de/~kkroeni/KLFitter/>.
- [28] <http://root.cern.ch>.
- [29] A. Caldwell, D. Kollar, K. Kroeninger. BAT - The Bayesian Analysis Toolkit. *arXiv:0808.2552v1 [physics.data-an]*, 2008.

- [30] R.J. Barlow. *Statistics - A Guide to the Use of Statistical Methods in the Physical Sciences*. WILEY, 1997.
- [31] L. Lyons. *Statistics for nuclear and particle physicists*. Cambridge University Press, 1986.
- [32] Extended Fits with Many Parameters such as Constrained Kinematic Fits.
http://www.desy.de/~csander/Talks/090401_ConstrainedFits.pdf.

Bibliography

List of Figures

2.1	$t\bar{t}$ production	9
2.2	Parton density functions	9
3.1	CERN accelerators	14
3.2	ATLAS detector	16
6.1	Energy resolution of b_{had} before fit	26
6.2	Energy resolution of b_{had} after first fit	28
6.3	Reconstruction efficiencies after first fit	30
6.4	Top masses after first fit	31
6.5	Distribution of $m_{t_{\text{had}}}$ after first fit	32
6.6	Estimated versus true JES	33
6.7	Gauss fit of JES	33
6.8	Calibration curve after first fit	34
6.9	Energy resolution of b_{had} after second fit	36
6.10	Reconstruction efficiencies after second fit	37
6.11	Top mass after second fit	38
6.12	Improvement of the energy resolution	39
A.1	Resolution of all measured energies	43
A.2	Resolution of all energies after first fit with BW	44
A.3	Resolution of all energies after first fit with EM	44
A.4	JES distribution BW	45
A.5	JES distribution EM	46
A.6	Calibration curve BW after first fit	47
A.7	Calibration curve EM after first fit	47
A.8	Calibration curve BW after second fit	48
A.9	Calibration curve EM after second fit	48

List of Figures

List of Tables

2.1	Mass and lifetime of leptons and quarks	4
2.2	Quantum numbers of fundamental particles	5
2.3	Gauge bosons	7
2.4	$q\bar{q}$ and gg contributions to $t\bar{t}$ production	10
2.5	Branching ratios of top decay	11
5.1	Fit constraints	23
6.1	Energy resolution of b_{had} before fit	27
6.2	Energy resolution of b_{had} after first fit	28
6.3	Fit parameters for JES	35
6.4	RMS of top mass distribution	38
6.5	Improvement of reconstruction efficiencies	40

List of Tables

Acknowledgements

First of all, I would like to thank Johannes Erdmann for supervising my bachelor's thesis so intensively. I am very grateful for the help concerning my questions about physics, statistics, programming, for the patience and expertise in conflicts with the CIP pool and batch system and for proof-reading at the latest moment.

I am much obliged to Dr. Kevin Kröniger for supervising my work, discussing the results and for the constructive suggestions in the proof-reading.

I would also like to thank Olaf Nackenhorst for his good advices, especially in the preceding Spezialisierungspraktikum.

It was a great luck to have three such motivated and helpful supervisors at once. Sincere thanks to the three of you again!

I am very thankful to Prof. Dr. Arnulf Quadt for motivating me to write my bachelor's thesis in particle physics, for encouraging me to participate in the summer student programm, for organising the physics show in this semester and, of course, for being the first referee. I would like to thank Prof. Dr. Ariane Frey for her willingness to be the second referee of this bachelors's thesis.

Special thanks to Andrea and Johannes that I could share the office in a nice atmosphere. Cordial thanks to Stefan for always knocking on the office door at lunch and coffee time and for answering my questions about the English language. Thank you to the whole second institute for welcoming us bachelor students.

Furthermore, I wish to express my gratitude to Steffen for his help with printing and Lena for handing in my thesis on time.

Erklärung nach §13(8) der Prüfungsordnung für den Bachelor-Studiengang Physik und den Master-Studiengang Physik an der Universität Göttingen:

Hiermit erkläre ich, dass ich diese Abschlussarbeit selbständig verfasst habe, keine anderen als die angegebenen Quellen und Hilfsmittel benutzt habe und alle Stellen, die wörtlich oder sinngemäß aus veröffentlichten Schriften entnommen wurden, als solche kenntlich gemacht habe.

Darüberhinaus erkläre ich, dass diese Abschlussarbeit nicht, auch nicht auszugsweise, im Rahmen einer nichtbestanden Prüfung an dieser oder einer anderen Hochschule eingereicht wurde.

Göttingen, den July 13, 2009

(Elina Fuchs)